Advances in Optics and Photonics

# High-order optical nonlinearities in plasmonic nanocomposites—a review

**ALBERT S. REYNA AND CID B. DE ARAÚJO***

*Departamento de Física, Universidade Federal de Pernambuco, 50670-901 Recife, PE, Brazil*
**Corresponding author: cidbdearaujo@yahoo.com.br*

*Received May 15, 2017; revised August 18, 2017; accepted August 21, 2017; published October 12, 2017 (Doc. ID 292084)*

Composites consisting of metal nanoparticles (NPs) embedded in dielectric media may present large nonlinear optical response due to electronic transitions in the NPs. When the metal NPs are suspended in liquids or embedded in solid substrates, the obtained composites may present high-order optical nonlinearities (HON) beyond the third-order nonlinearity, usually studied for most materials. Moreover, it is observed that the magnitude and phase of the effective high-order susceptibilities can be controlled by adjusting the light intensity, $I$, and the volume filling fraction, $f$, occupied by the NPs. Therefore, the sensitivity to the values of $I$ and $f$ allowed the development of a *nonlinearity management* procedure for investigation and control of various phenomena, such as self- and cross-phase modulation, spatial modulation instability, as well as bright and vortex solitons stabilization, in media presenting relevant third-, fifth-, and seventh-order susceptibilities. As a consequence, it is reviewed in this paper how the exploitation of HON in metal–dielectric nanocomposites may reveal new ways for optimization of all-optical switching devices, light-by-light guiding, as well as the control of solitons propagation for long distances. Also, theoretical proposals and experimental works by several authors are reviewed that may open the possibility to identify new high-order phenomena by applying the *nonlinearity management* procedure. Therefore, the paper is focused on the properties of metal nanocomposites and demonstrates that these plasmonic composites are versatile platforms for high-order nonlinear optical studies.

OCIS codes: (160.4330) Nonlinear optical materials; (350.4238) Nanophotonics and photonic crystals; (190.3270) Kerr effect; (190.4420) Nonlinear optics, transverse effects in; (190.5940) Self-action effects; (190.6135) Spatial solitons
https://doi.org/10.1364/AOP.9.000720

1. Introduction . . . . . . . . . . 722
2. Optical Properties of Metal Nanoparticles . . . . . . . . . . 723
3. Optical Nonlinearity of Spherical Nanoparticles Suspended in a Liquid . . 730
4. Maxwell–Garnet Metal–Dielectric Nanocomposites . . . . . . . . . . 731
5. Nonlinearity Management Procedure to Exploit High-Order Nonlinearities. . . 733
    5.1. Scope and Limitations of the Nonlinearity Management in Metal–Dielectric Nanocomposites . . . . . . . . . . 734

6. Applications of the Nonlinearity Management Procedure . . . . . . . . . . . . 736
  6.1. Spatial Self-Phase Modulation . . . . . . . . . . . . . . . . . . . . . . . . . . . . 736
  6.2. Spatial Modulation Instability . . . . . . . . . . . . . . . . . . . . . . . . . . . . 738
  6.3. Bright and Vortex Solitons . . . . . . . . . . . . . . . . . . . . . . . . . . . . . 741
  6.4. Polarization Instability Due to High-Order Nonlinearities . . . . . . . . . 746
  6.5. All-Optical Switches Based on Metal–Dielectric Nanocomposites . . . 748
7. Foreseen Advances in the Study of High-Order Optical Phenomena . . . . . 750
  7.1. Stability Conditions for One-Dimensional Optical Solitons in Cubic–Quintic–Septimal Media . . . . . . . . . . . . . . . . . . . . . . . . . . 750
  7.2. Low-Intensity Excitation of Plasmonic Solitons in Metal Nanocolloids 751
  7.3. Nonlinearity Management in Plasmonic Metamaterials. . . . . . . . . . . 754
8. Conclusions and Outlook . . . . . . . . . . . . . . . . . . . . . . . . . . . . . . . . . 760
Funding . . . . . . . . . . . . . . . . . . . . . . . . . . . . . . . . . . . . . . . . . . . . 761
Acknowledgment . . . . . . . . . . . . . . . . . . . . . . . . . . . . . . . . . . . . . . . 761
References . . . . . . . . . . . . . . . . . . . . . . . . . . . . . . . . . . . . . . . . . . 761

# High-order optical nonlinearities in plasmonic nanocomposites—a review

**Albert S. Reyna and Cid B. de Araújo**

## 1. INTRODUCTION

The behavior of metal–dielectric nanocomposites (MDNCs)—dielectric hosts with embedded metal nanoparticles (NPs)—is receiving much attention at the present time and far-reaching consequences of technological developments are foreseen in the future. Currently, highly nonlinear (NL) MDNCs can be fabricated using a large variety of methods [1–7]. As a result, the study of optical properties of MDNCs has been a topical theme in the past few years aiming at their application in devices such as lasers, color displays, plasmonic solar cells, channel waveguides, among other applications. In addition, both linear and NL optical properties of the MDNCs can be enhanced by orders of magnitude if a judicious selection of host and metallic NPs is made.

The NL optical response of MDNCs can be described by the induced electrical polarization as a power series of the incident electric field with effective susceptibilities, $\chi_{\text{eff}}^{(N)}$, $N = 1, 2, 3, \ldots$, as the coefficients of the series expansion, analogously to the conventional description for homogeneous materials [8]. Accordingly, in systems with inversion symmetry, due to the vector character of the electric polarization, all even-order susceptibilities are null. Therefore the NL response of centro-symmetric composites is associated with the odd-order nonlinear susceptibilities, $\chi_{\text{eff}}^{(2N+1)}$, $N = 1, 2, 3, \ldots$, that include contributions of the host material and the NPs. In addition, $\chi_{\text{eff}}^{(2N+1)}$ depends on the mismatch between the dielectric functions of the NPs and the host, and the excitation of localized surface plasmons (LSPs) of the NPs [9] may enhance the NL response of the MDNCs by orders of magnitude.

A large number of centro-symmetric MDNCs presents high-order nonlinearities (HONs) that can be investigated even using lasers of moderate intensities. For example, in the case of metal nanocolloids or glasses doped with metallic NPs, it is possible to detect phenomena up to the seventh order using lasers with intensities of few $\text{GW/cm}^2$ in diluted samples containing NPs that occupy volume fractions of $10^{-5} < f < 10^{-4}$ as illustrated in this paper. The effective NL susceptibilities depend on the nature, shape and sizes of the NPs; the value of $f$; the laser wavelength, $\lambda$; and the mismatch between the complex dielectric functions of the NPs, $\varepsilon_{\text{NP}}$, and their host, $\varepsilon_h$. Larger optical response can be observed when the optical frequency is near the LSP resonance frequency, $\omega_{\text{LSP}}$.

From the basic point of view MDNCs are interesting physical systems, because their electronic response can be understood and controlled by changing $f$, the light intensity, $I$, and the NP host. For a given host, by changing $f$ and/or $I$ it is possible to observe and control constructive or destructive interferences between NL optical susceptibilities of different orders. This *nonlinearity management* procedure enables the preparation of samples with the total effective susceptibility controlled at will as, for example, the fabrication of a MDNC with suppressed $\text{Re}\,\chi_{\text{eff}}^{(3)}$ and enhanced $\text{Re}\,\chi_{\text{eff}}^{(2N+1)}$ with $N \geq 2$.

In this paper we review and discuss HON assisted phenomena in MDNCs consisting of metal nanocolloids. Several phenomena will be investigated including: (*i*) the observation of spatial modulation instability due to the quintic nonlinearity; (*ii*) the spatial self- and cross-phase modulation (XPM) due to quintic and septimal nonlinearities; (*iii*) the observation of bright spatial solitons propagating in a medium managed to present fifth-seventh (focusing–defocusing) refractive nonlinearity with suppressed third-order refractive index; (*iv*) an optimization procedure for design of ultrafast all-optical switches (AOSs) based on MDNCs; (*v*) the observation of light confinement and guiding induced by an optical vortex soliton in a cubic–quintic (defocusing–focusing) metal nanocolloid. Studies on the polarization instability of an optical field propagating in a medium with HON will also be presented as well as results related to the stability of optical vortices propagating in metal nanocolloids with managed nonlinearity.

The data reported are compared with analytical and numerical calculations including HON with dissipative terms related to multiphoton absorption processes. The samples' parameters used for numerical simulations were obtained from independent experiments and good agreement between the theoretical and numerical results with the experimental data are presented.

The paper is organized as follows. In Section 2, we briefly review the optical properties of metallic NPs considering their intrinsic behavior as well as the influence of the dielectric host on their optical response. In Section 3 we discuss the origin of the NP nonlinearity, the influence of the environment on the optical behavior of silver nanocolloids, and a comment is made on the experiments to measure the susceptibilities associated to HON. In Section 4 we present an effective medium approximation to describe the NL optical properties of metal nanocolloids which are the prototypes of the MDNCs of our main interest. In Section 5 we discuss a *nonlinearity management* procedure to control HON in MDNCs. In Section 6 we present experiments analyzed with basis on the standard formalism of nonlinear optics with samples prepared by *nonlinearity management*. In Section 7 the possibility of new studies based on theoretical proposals and recent experiments by various authors are discussed aiming at the extension of the *nonlinearity management* procedure in new directions. Finally, in Section 8 we present a summary of the main results and a discussion of possible future works with nonlinear MDNCs.

## 2. OPTICAL PROPERTIES OF METAL NANOPARTICLES

The optical properties of metal NPs have been exploited from time immemorial in sculptures and paintings. The most famous example is the Lycurgus cup (4th century AD) that is exposed in the British Museum of London. The cup is a decorative Roman artifact made of a dichroic glass containing gold–silver alloyed NPs that reflects (transmits) green (red) when illuminated with white light. In the Middle Age the Roman glass-manufacturing technology became widespread and stained glass was used in many churches, monuments, and pottery objects. However, the first scientific study is attributed to Faraday that was able to prepare stable colloidal gold and recognized their beautiful colors as due to the suspended particles in the liquid [10]. The ability to characterize the particles in colloids and in solid-state MDNCs, such as in the Lycurgus cup, was developed with the invention of transmission electron microscopy, atomic force microscopy, scanning tunneling microscopy, and other modern techniques in the 20th century.

From a classical point of view the optical response of the NPs can be described using the Mie theory [11] that enables calculation of the NPs' extinction coefficient considering its complex dielectric function, $\varepsilon_{\mathrm{NP}}$, embedded in a host presenting the dielectric function $\varepsilon_h$. In a microscopic description we consider that noble metal NPs exhibit large optical response due to the interaction of the electrons with the optical field and the relevant physical processes are: (*i*) transitions associated with the conduction band electrons (intraband transitions), and (*ii*) electron transitions from the valence to the conduction band (interband transitions). For silver NPs, for example, the dominant electronic transitions can be understood by examining the bulk band structure. It can be concluded that for photon energies up to ~2 eV the light absorption is dominated by intraband transitions. For photons of ~3 eV the main contribution for optical absorption is due to the LSP resonance, while for photon energies larger than ~4 eV the interband transitions strongly influence the optical response.

The contribution of intraband transitions for $\varepsilon_{\mathrm{NP}}$ can be understood using the Drude model with an additional term describing the high frequency part, $\varepsilon^{ib}$ (associated with the interband transitions) [12], by the expression

$$\varepsilon_{\mathrm{NP}}(\omega) = \varepsilon^{ib} - \frac{\omega_p^2}{\omega^2 + i\gamma\omega}, \tag{1}$$

where $\omega$ is the angular frequency of light, $\omega_P = \sqrt{Ne^2/\varepsilon_0 m_e}$ is the bulk plasma frequency, $N$ is the density of free electrons, $e$ is the electron charge, $\varepsilon_0$ is the vacuum permittivity, $m_e$ is the electron effective mass, and $\gamma = v_f/R_{\mathrm{bulk}}$ is the electron collision frequency, with $v_f$ being the Fermi velocity and $R_{\mathrm{bulk}}$ the mean-free-path of conduction electron in the metal. $\varepsilon^{ib}$ is an empirical parameter that allows tuning of the resonance on a wide frequency range in order to match the theoretical with experimental results. The contribution of the interband transitions can be understood physically by adding the Lorentzian terms into the Drude expression (Drude–Lorentz model), given by [13]

$$\varepsilon_{\mathrm{NP}}(\omega) = 1 - \frac{f_0\omega_p^2}{\omega^2 + i\gamma_0\omega} - \sum_{j=1}^{m} \frac{f_j\omega_p^2}{(\omega^2 - \omega_j^2) + i\gamma_j\omega}, \tag{2}$$

where $m$ corresponds to the total number of the oscillators, each with lifetime $\gamma_j$, strength $f_j$, and modified plasma frequency $\sqrt{f_j}\omega_p$. Figure 1 shows a comparison between experimental (black points) and theoretical (solid lines) results of the dielectric function of semitransparent gold films with thickness of 250 Å. The theoretical analysis was performed using the Drude model, considering $\varepsilon^{ib} = 1$ (blue line) and $\varepsilon^{ib} = 11.5$ (red line), and the Drude–Lorentz model (green line). In both the real and imaginary parts of the dielectric function, the Drude–Lorentz model is able to adequately reproduce the experimental results in the UV-visible region by adding the contributions of interband transitions.

Figure 1

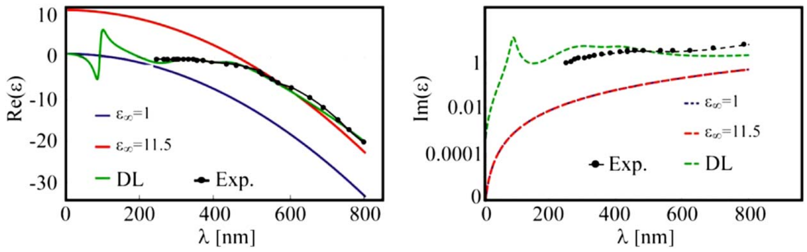

Real and imaginary parts of the dielectric function of a thin semitransparent gold film. Comparison between Drude model with $\varepsilon^{ib} = 1$ (blue lines), $\varepsilon^{ib} = 11.5$ (red lines), Drude–Lorentz (DL, green lines), and experimental data (black points). Reprinted with permission from [14]. Copyright 2013 MDPI.

When the NPs' dimensions are much smaller than $\lambda$, the light field is uniform across the particle and the collective electrons oscillation is described by a dipolar polarizability represented by

$$\alpha = (1+\eta)\varepsilon_0 V \frac{(\varepsilon_{\mathrm{NP}} - \varepsilon_h)}{(\varepsilon_{\mathrm{NP}} + \eta\varepsilon_h)}, \tag{3}$$

where $V$ is the NP volume and $\eta$ is a geometric factor that depends on the NP shape ($\eta = 2$ for spherical NPs but assumes larger values for particles with different geometry) [15]. When $\mathrm{Re}(\varepsilon_{\mathrm{NP}} + \eta\varepsilon_h) = 0$, the polarizability of the NPs becomes maximum and the corresponding frequency is the LSP resonance frequency, $\omega_{\mathrm{LSP}}$, given by

$$\omega_{\mathrm{LSP}} = \sqrt{\frac{Ne^2}{m_e\varepsilon_0 \,\mathrm{Re}(\varepsilon^{ib} + \eta\varepsilon_h)} - \gamma^2}. \tag{4}$$

The LSP has a hybrid electromagnetic wave and surface charge character giving origin to a field component (perpendicular to the NP surface) that decays exponentially with distance from the NP. The excitation of LSP occurs in the ultraviolet-to-near-infrared region for interfaces between metal and dielectrics (glass, water, air, polymers, etc.). The LSP resonance frequency of nonspherical NPs is generally smaller than the LSP frequency of spherical NPs [9,15]. Notice from Eq. (4) that the LSP resonance wavelength is redshifted when the particles are embedded in a host with larger $\mathrm{Re}(\varepsilon_h)$ (corresponding to large linear refractive index, $n_0$).

The absorptive response, described by $\mathrm{Im}(\varepsilon_{\mathrm{NP}})$, is mainly due to electron–phonon collisions and electron-surface scattering [9]. Radiative decay of energy is relevant only for large particles with sizes comparable with the light wavelength. Thus, solving the problem of absorption and scattering of light by a small particle involves solving Maxwell's equations with the correct boundary conditions. For the particular case of spherical nanoparticles, according to Mie theory [16], assuming a negligible value of $\mathrm{Im}[\varepsilon_h(\omega)]$, the NP optical extinction coefficient has the form

$$\alpha_{\mathrm{ext}} = \frac{18\pi V_{\mathrm{NP}}}{\lambda}[\varepsilon_h(\omega)]^{3/2} \frac{\mathrm{Im}[\varepsilon_{\mathrm{NP}}(\omega)]}{(\mathrm{Re}[\varepsilon_{\mathrm{NP}}(\omega)] + 2\varepsilon_h(\omega))^2 + \mathrm{Im}[\varepsilon_{\mathrm{NP}}(\omega)]^2}, \tag{5}$$

where $V_{\mathrm{NP}}$ is the particle volume and $\alpha_{\mathrm{ext}}$ describes contributions from absorption and light scattering. However, for particles with dimensions much smaller than $\lambda$, the light scattering is not relevant [17]. Equation (5) shows that the extinction coefficient is influenced by the particle size only with respect to its amplitude. However, experimental studies show that the position and bandwidth of the LSP resonance varies with the particles shape and size, when the particle dimensions are smaller than the electrons mean-free-path. Therefore, Mie theory was modified to introduce a size dependence of the dielectric function of spherical metal NPs, $\varepsilon_{\mathrm{NP}}(\omega, R)$, where the particle radius, $R$, was introduced in the electron collision frequency $\gamma = \gamma_{\mathrm{bulk}} + v_f/R$. Thus, based on the Mie theory and by using the Drude–Lorentz model considering the limitations of the mean-free-path, it is possible to observe that the LSP resonance wavelength shifts toward the blue region as the particle size is reduced, followed by broadening of the LSP bandwidth.

Figure 2 illustrates the extinction coefficient of gold NPs, with different sizes, calculated using the Mie theory [Eq. (5)], based on the Drude model [Eq. (1)] and Drude–Lorentz model [Eq. (2)]. Figures 2(a) and 2(b) show that both models behave analogously for energies smaller than 1.6 eV and exhibit good agreement with the experimental results shown in Fig. 2(c). However, for the spectra with extinction peaks of larger frequencies, corresponding to smaller NPs, the Drude–Lorentz model provides better results in comparison with the experimental data due to the interband transitions contributions.

Also with the purpose of explaining the size dependence of the LSP resonance in metal NPs, different quantum models were developed that also predict the $1/R$ dependence of the electron relaxation rate [12,16,18–23]. These models assume that the particle dimensions are comparable to the Fermi wavelength of the electrons and consequently the electronic motion is spatially confined with the electronic energies assuming a discrete set of values; such an effect is commonly known as *quantum confinement*.

In addition, the extinction spectra of metal NPs may provide information on the kind of metal being studied, as well as the size and shape of the particles. In order to proceed with such an analysis it is needed to identify three important characteristics from the spectrum: (*i*) the full width at half-maximum, (*ii*) the LSP resonance frequency, and (*iii*) the amplitude of the LSP resonance curve. In [24] the authors illustrate how the LSP band and the contributions due to interband and intraband transitions may contribute for the spectrum profile. For different metals the LSP resonance frequency and the contribution of interband transitions on the optical absorption spectrum are different. For silver NPs both transitions do not overlap, whereas for gold NPs the contributions of interband and intraband transitions are superimposed [25]. Nonetheless, by a careful analysis of the spectrum and by using Mie theory it is possible to estimate the particles size (assuming a spherical shape), but one should be aware that the particle size determined in this way is sensitive to the LSP resonance line shape. It is also well known that the size dispersion of the NPs in an ensemble

Figure 2

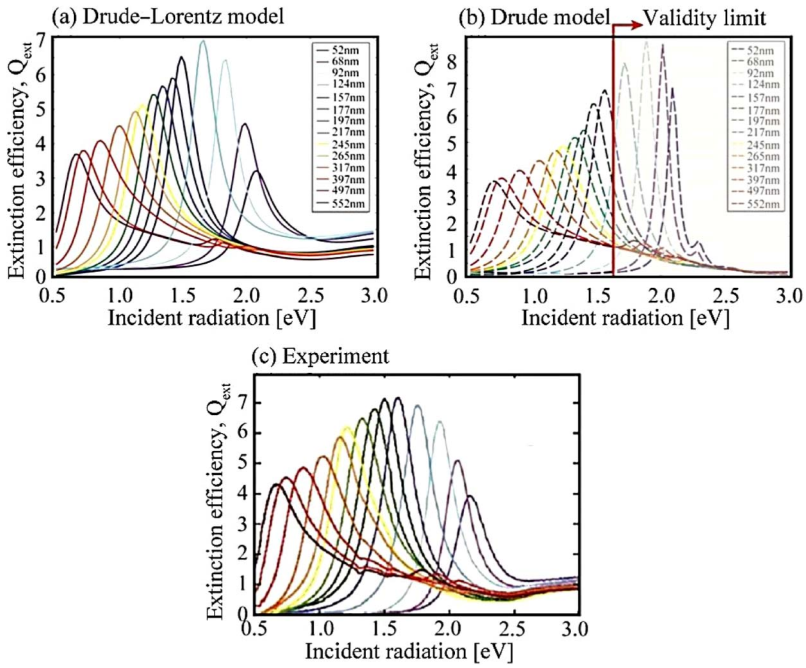

(a),(b) Theoretical and (c) experimental extinction efficiency of gold NPs having different diameters. (a) Drude–Lorentz model and (b) Drude model with $\varepsilon^{ib} = 11.5$. Adapted with permission from [14]. Copyright 2013 MDPI.

produces broadening of the LSP absorption band and deviation from the NP sphericity shifts the LSP resonance to larger wavelengths.

For an individual NP the electric field in its vicinity is the sum of the incident field, $E_0$, plus the field generated by the electrons oscillation. At the NP surface, in the dipolar limit, the field is

$$E_{\mathrm{NP}} = \frac{(1+\eta)\varepsilon_h}{(\varepsilon_{\mathrm{NP}} + \eta\varepsilon_h)} E_0. \tag{6}$$

For a silver NP with a diameter of 20 nm the intensity enhancement, $|E_{\mathrm{NP}}|^2/|E_0|^2$, due to the LSP resonance can reach $\sim 10^4$. Then, the electronic transitions of atoms or molecules located in the proximity of the NPs, with frequency around $\omega_{\mathrm{LSP}}$, can be largely enhanced as observed, for example, in processes such as optical absorption and photoluminescence [26] and harmonic generation and surface Raman scattering [27]. However, as the particle size increases the intensity enhancement reduces.

For nonspherical particles the intensity enhancement can be much larger than for a spherical NP due to the "lightning rod effect" [28].

Presently, various chemical and physical techniques are available for fabrication of noble metal NPs having a large variety of shapes, such as nanoprisms, nanoshells, nanorods, etc., and the corresponding LSP frequencies span the whole visible and near-infrared spectrum as indicated in Fig. 3 [29].

Figure 4 shows the two plasmon bands related to the transverse and longitudinal electron oscillations in nanorods [30]. The aspect ratio (longitudinal dimension/transverse dimension) is an important parameter to characterize the optical properties of such particles. The relative amplitude of the bands depends on the aspect ratio; the longitudinal (transverse) LSP wavelength is blueshifted (redshifted) when the aspect ratio is increased [30,31]. It is important to notice that even small deviations from the spherical shape may produce large color changes in the particles.

The calculated polarizability, extinction cross section, and the polarizability tuning spectra are shown in Fig. 5 for aqueous solution of gold nanorods with an aspect ratio equal to 2 and for silica–gold core–shell particles with a shell thickness of 15 nm [32].

Figure 3

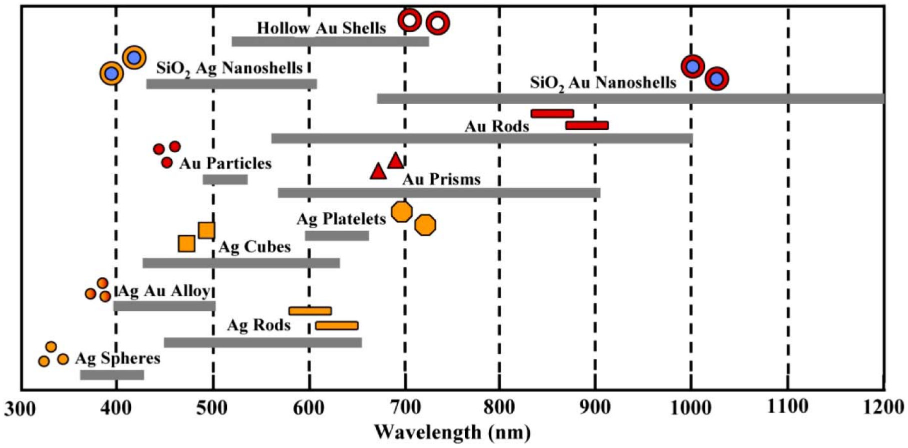

Tuning the LSP wavelengths by varying the size and shape of the nanoparticles. Reprinted with permission from [29]. Copyright 2007 SPIE.

Figure 6 shows the colors and absorption spectra of silver nanoprisms with various dimensions, prepared by illuminating spherical NPs using different wavelengths in order to shape the particles in an appropriate way [33].

Figure 4

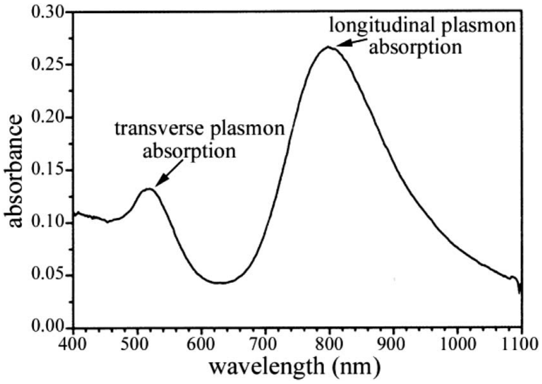

Absorbance of a colloid containing gold nanorods (aspect ratio: 4.1). Reprinted with permission from Link and El-Sayed, J. Phys. Chem. B, **103**, 8410–8426 (1999) [30]. Copyright 1999 American Chemical Society.

Figure 5

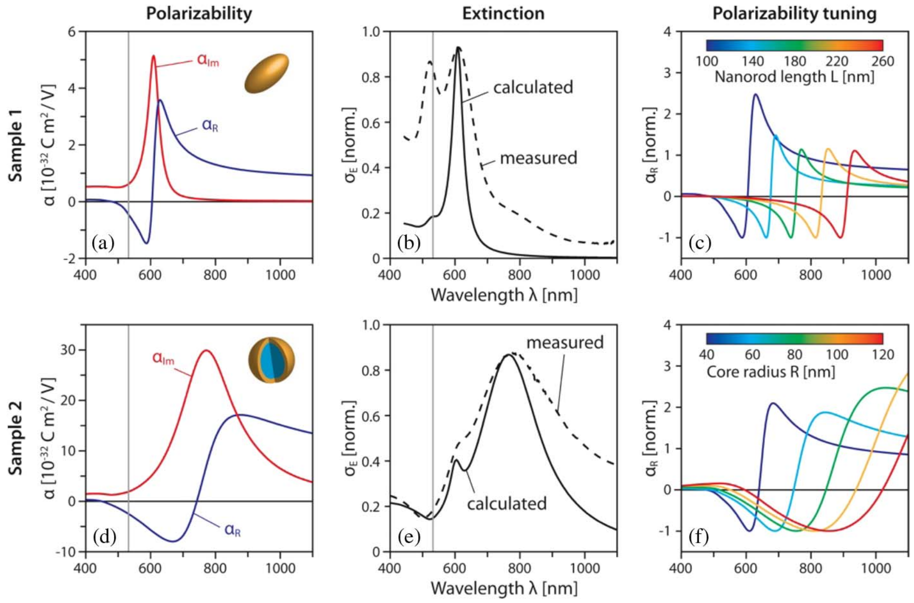

Calculated polarizability of (a) gold nanorods—sample 1 (length: 100 nm; width: 50 nm) and (d) silica–gold core–shell particles—sample 2 (core radius: 60 nm; shell thickness: 15 nm) suspended in water. The blue and red curves represent the real and imaginary parts of the polarizability, $\alpha_R$ and $\alpha_{\text{Im}}$, respectively. The calculated and measured normalized extinction cross section for samples 1 and 2 are shown in (b) and (e), respectively. (c) Tunability of $\alpha_R$ for gold nanorods as a function of the rod length with a fixed width of 50 nm. (f) Tuning of $\alpha_R$ for silica–gold core–shell particles similar to those in sample 2 as a function of the silica core size for a fixed shell thickness of 15 nm. The vertical lines indicate the wavelength at 532 nm. Reprinted with permission from Fardad *et al.*, Nano Lett. **14**, 2498–2504 (2014) [32]. Copyright 2014 American Chemical Society.

For particles with dimensions comparable (or larger) to the light wavelength the field across the particle is nonuniform. Then, two effects should be considered: (*i*) the phase retardation that broadens the dipole resonance, and (*ii*) the presence of multipole resonances that can be excited even in spherical NPs [34]. Different approaches are available for calculation of the absorption spectrum, polarizability, extinction coefficient, and intensity enhancement corresponding to NPs with different sizes, geometrical shapes, and when they are interacting with other NPs [28,34]. Among the most commonly used methods to compute scattering and absorption of electromagnetic waves by particles of arbitrary geometry, different sizes and composition are the Mie Theory [11,16], discrete dipole approximation (DDA) [35], finite-difference time-domain (FDTD) [36], and Whitney form finite element (WF-FE) method [37]. The choice of the method to be used depends on the NP characteristics [38]. For example, Mie theory shows large limitations to nonspherical particles which can be adequately modeled using the other three methods. In general, the DDA, FDTD, and WF-FE methods simulate the particles using discrete elements (cubic for DDA and FDTD, and tetrahedral for WF-FE) small compared to the particle size but large compared to the size of an atom. Numerical calculations show that the DDA method is more sensitive to refractive index shifts [39]. Small changes in the DDA method to incorporate the existence of multipoles in the calculations allow the use of this model for a wide variety of particle shapes, sizes, and refractive indices [34,40]. The numerical simulations based on the DDA method (for example, discrete dipole scattering [41]) present errors usually smaller than 10%, mainly at positions near the particle surface [35]. The FDTD method is a more general and accepted method that provides more exact results but it demands long simulations to avoid phase errors due to the discretization intervals. The same limitation is observed for the WF-FE method, but more exact results can be obtained mainly in positions near the particle surfaces. Other methods for different nanostructures are reported in the literature [42–45].

Concerning the optical properties of very small metal NPs due to the quantum confinement effects, the time-dependent density functional theory (TDDFT) [46] based on the jellium model presents satisfactory results for the plasmon energies of small NPs and

Figure 6

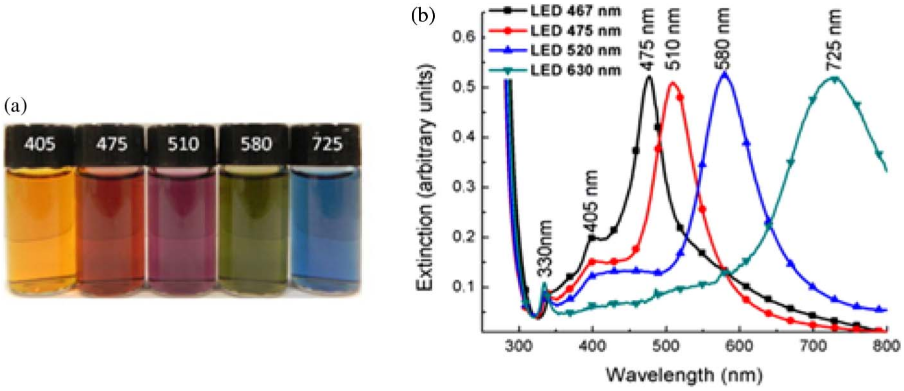

(a) Photograph shows the colors of aqueous colloids containing silver nanoprisms with average sizes from 30 to 150 nm. The yellow sample was not irradiated and contains the NPs used as seeds for the nanoprisms preparation. The numbers in the vials indicate the light wavelength used to shape the nanoprisms. (b) Extinction spectra exhibiting the normalized absorption bands for the samples irradiated by LEDs with emission wavelengths indicated in the inset. Reprinted with permission from [33]. Copyright 2014, with permission from Elsevier.

good agreement with experimental results for metal nanocluster with few atoms [47]. It is important to emphasize that the TDDFT is applicable to NPs with different shapes [48,49].

The design and fabrication of metallic nanostructures with tunable LSP resonances is described, for example, in [1,7,29,50] with comments on several potential photonic applications.

## 3. OPTICAL NONLINEARITY OF SPHERICAL NANOPARTICLES SUSPENDED IN A LIQUID

The interest in the NL properties of metal nanocolloids increased after demonstration of the giant enhancement of the effective third-order susceptibility owing to the contribution of local field effects [51,52]. In these papers the authors measured the third-order response of gold NPs either in aqueous solutions or embedded in silica glass. They have shown that the fast nonlinearity is enhanced due to the proximity between the laser and LSP frequencies and developed a model to describe the resonant enhancement. Besides the characterization of the NL response as due to electronic transitions in the NPs, they report that the third-order susceptibility of the samples varied with the inverse of the third power of the NP radius.

Presently it is known that the optical response of metal NPs is highly influenced by their environment since the majority of the atoms are in the NPs–host interface. For example, for a spherical silver NP with a diameter of 4 nm, about 30% of the atoms are in the surface. The influence of the environment on the NP linear optical behavior was investigated in the past (see, for example, [16,53]), but up until recently not many systematic studies were reported with respect to the dependence of the effective NL susceptibility. In the case of silver nanocolloids the experiments reported in [54,55] demonstrated quantitatively the influence of molecules attached to the NP surface as well as the sensitivity of the NL response to the solvent where the particles were suspended. The optical dephasing of the LSP is also very sensitive to the different capped molecules on the NP surface [56]. More recently this effect was investigated for individual NPs [57] and a good understanding of the surface broadening effects and their morphology dependence was obtained.

The experimental results of [12,58] were understood considering the size dependence of $\varepsilon_{\mathrm{NP}}(\omega)$ described by an empirical model [59,60] which assumes that for a NP with radius $R$ smaller than the bulk electron mean-free-path, the dielectric function is given by $\varepsilon_{\mathrm{NP}}(\omega) = \varepsilon_{\mathrm{bulk}}(\omega) + i\left(\frac{\omega_{\mathrm{LSP}}^2}{\omega^3}\right)\left(\frac{A v_F}{R}\right)$, where $v_F$ is the Fermi velocity and $A$ is a phenomenological parameter that depends on the NP shape and the NPs–host interface because the NPs in a colloid have to be capped by adsorbed molecules (AMs) to prevent their aggregation. The bulk electron mean-free-path in silver is 53.3 nm and it is 37.7 nm in gold [61].

The influence of the stabilizing agents and solvents on the NL susceptibility of nanocolloids with silver NPs capped with sodium citrate, poly(N-vinylpyrrolidone), and polyvinyl alcohol in aqueous solutions, methanol, acetone, and ethylene glycol was discussed in [54,55]. The colloids were prepared following the method introduced by [62] and the size homogeneity of the NPs was obtained by laser ablation following the procedure described in [63]. The results achieved using the Z-scan technique [64] showed variations of $\chi_{\mathrm{NP}}^{(3)}$ up to ~300% by changing either the AM or the host solvent. The influence of the stabilizing agents was understood recalling that the AM originate dipolar layers on the NP surface that interact with the electromagnetic field and the effect of the solvent is due to the electric dipole moment of the molecules in the solvent that affect very much the electron density of states of the NPs and the local field in the proximity of the NPs. Details of the experiments and a discussion on the results are given in [54,55] with the particles being considered as metallo-organic complexes.

Many publications related to the basic characteristics of metal nanocolloids and solid-state metal composites appeared in the past years [65–78]. In the majority of the experiments the authors focused on the third-order properties of the materials. The area is still very active and studies of MDNCs based on glasses and colloids were reported by many authors concerning the NL behavior of other metals than silver and gold as well as other NP geometries. The two NL optical techniques mostly used were the pump-and-probe and the Z-scan technique in various versions, as described in [79]. Although the environment influence has not been much considered, its influence may be one of the reasons for scattering of the values reported for silver and gold MDNCs.

The HON of diluted silver colloids was revealed not long ago [67,80,81] and systematic studies to exploit the HON of silver nanocolloids were reported in the past three years. A discussion based on such experiments will be presented in the following sections.

## 4. MAXWELL–GARNET METAL–DIELECTRIC NANOCOMPOSITES

One approach to describe the optical properties of MDNCs consists of assuming the NPs and their host as a homogeneous medium having an effective complex dielectric function, $\varepsilon_{\text{eff}}$. Although several effective medium models can be used to understand the physical properties of composites [82–86], we will consider here the Maxwell–Garnet model, which is very appropriate to describe the two-phase mixture effective dielectric function, $\varepsilon_{\text{eff}}$, represented by MDNCs with small concentration of isolated metallic NPs suspended in a dielectric host. Then, considering NPs with diameter $a$ smaller than their relative distance $b$, $a < b < \lambda$, and assuming no interactions among the NPs, the complex effective dielectric function is obtained from

$$\frac{\varepsilon_{\text{eff}} - \varepsilon_h}{\varepsilon_{\text{eff}} + 2\varepsilon_h} = f\,\frac{\varepsilon_{\text{NP}} - \varepsilon_h}{\varepsilon_{\text{NP}} + 2\varepsilon_h}, \tag{7}$$

where $f$ is the volume filling fraction (the volume fraction of the sample occupied by the NPs).

To describe MDNCs with larger filling fractions than the ones considered in this work, other approaches have been used. For instance, the Bruggeman model [87] emerges as a homogenization approach to analyze more than one type of inclusion with concentrations having the same order of magnitude in the MDNC. This method is particularly adequate to describe the optical properties of MDNCs at the percolation threshold, where the conductivity becomes nonzero. However, for large volume fractions the LSP resonance cannot be described by the Bruggeman model [88].

Some extensions are available to the Maxwell–Garnet model to analyze mixtures with anisotropic inclusions [89] and even consider the influence of particle interactions on the local electric field [90]. Other models, such the coherent-potential approximation [91] and power-law approximation (Birchak model [92] and Looyenga model [93]), are also used to model the dielectric function of MDNCs adapted to different conditions.

In nonlinear optics, the Maxwell–Garnet model was originally applied to describe the effective third-order optical susceptibility, $\chi^{(3)}_{\text{eff}}$, of a composite in [94], where the authors were able to demonstrate its validity for a large range of $f$ values. The model was successfully applied to interpret the results of third-order experiments with metal nanocolloids and solid-state MDNCs [95–97]. More recently the Maxwell–Garnet model was extended to include the contributions of $\chi_{\text{eff}}^{(3)}$, $\chi_{\text{eff}}^{(5)}$, and $\chi_{\text{eff}}^{(7)}$, considering $f \ll 1$ and spherical NPs [98]. Other models, such as the generalized $T$-matrix approach [99] and two-temperature model for hot electrons [81], may be used in order to identify HON contributions in metal NPs. However, both models were used to derive expressions for the high-order susceptibilities from the third-order nonlinearity (cascade-like contributions) neglecting the intrinsic NP susceptibilities.

The generalized Maxwell–Garnet model was developed considering the optical polarization in the quasi-static approximation as $P = P_h + \frac{1}{V}\sum_{i=1}^{Np} p_i$, where $P_h$ is associated with the host; $N_p$ is the number of NPs inside the volume $V$; $p_i = 3v_i\beta\varepsilon_h E_0$, where $v_i$ is the NP volume; $\beta = \frac{\varepsilon_{\text{NP}}-\varepsilon_h}{\varepsilon_{\text{NP}}+2\varepsilon_h}$, and $E_0$ is the optical field. Therefore the optical polarization is written as

$$P = \varepsilon_h^L \left\{ \frac{\varepsilon_h}{\varepsilon_h^L} \left[ \chi_h + \frac{3\beta f}{1-\beta f} \right] \right\} E_0 = \varepsilon_h^L \chi(|E_0|^2) E_0, \tag{8}$$

where $\chi_h$ is the host susceptibility.

Expressions for $\varepsilon_{\text{NP}}$ and $\varepsilon_h$ were obtained as a sum of the linear and NL contributions as $\varepsilon_{h,\text{NP}} = \varepsilon_{h,\text{NP}}^{(L)} + \varepsilon_{h,\text{NP}}^{(\text{NL})}$, where $\varepsilon_{h,\text{NP}}^{(L)}$ represent the linear part of the dielectric function, described through Eqs. (1)–(7), and the NL terms are

$$\varepsilon_{\text{NP}}^{(\text{NL})} = \varepsilon_h^{(L)} \left[ \frac{3}{4}\chi_{\text{NP}}^{(3)} \langle |E_{\text{NP}}|^2 \rangle + \frac{5}{8}\chi_{\text{NP}}^{(5)} (\langle |E_{\text{NP}}|^2 \rangle)^2 + \frac{35}{64}\chi_{\text{NP}}^{(7)} (\langle |E_{\text{NP}}|^2 \rangle)^3 \right], \tag{9}$$

$$\varepsilon_h^{(\text{NL})} = \varepsilon_h^{(L)} \left[ \frac{3}{4}\chi_h^{(3)} \langle |E_0|^2 \rangle + \vartheta(E_0) \right], \tag{10}$$

where $\langle |E_i|^2 \rangle$, $i = 0, \text{NP}$, correspond to the mean square modulus of the electric field and the numerical coefficients of both equations correspond to the degeneracy factors for the $i$-th order process according to the convention of [100]. The term $\vartheta(E_0)$ corresponds to the HON of the host. Considering $f \ll 1$ and expressing $\varepsilon_{\text{eff}}$ as a power series of $\langle |E_0|^2 \rangle$, we obtain

$$\chi_{\text{eff}}^{(3)} = f L^2 |L|^2 \chi_{\text{NP}}^{(3)} + \chi_h^{(3)}, \tag{11}$$

$$\chi_{\text{eff}}^{(5)} = f \left[ L^2|L|^4\chi_{\text{NP}}^{(5)} - \frac{6}{10}L^3|L|^4(\chi_{\text{NP}}^{(3)})^2 - \frac{3}{10}L|L|^6|\chi_{\text{NP}}^{(3)}|^2 \right], \tag{12}$$

$$\begin{aligned}\chi_{\text{eff}}^{(7)} = f \Big\{ & L^2|L|^6\chi_{\text{NP}}^{(7)} + \frac{12}{35}L^4|L|^6(\chi_{\text{NP}}^{(3)})^3 - \frac{3}{35}|L|^8[4|L|^2\chi_{\text{NP}}^{(3)} + |L|^2(\chi_{\text{NP}}^{(3)})^*]|\chi_{\text{NP}}^{(3)}|^2 \\ & - \frac{4}{7}L|L|^6[2\,L^2\chi_{\text{NP}}^{(3)} + |L|^2(\chi_{\text{NP}}^{(3)})^*]\chi_{\text{NP}}^{(5)} \Big\},\end{aligned} \tag{13}$$

where $L = 3\varepsilon_h^{(L)}/(\varepsilon_{\text{NP}}^{(L)} + 2\varepsilon_h^{(L)})$. The terms proportional to $f^n$, $n \geq 2$, were neglected as well as the fifth- and seventh-order contributions due to the host.

Since $L$ is a complex number, Eqs. (11)–(13) show that the values of both $\text{Re}\chi_{\text{eff}}^{(2N+1)}$ (refractive nonlinearity) and $\text{Im}\chi_{\text{eff}}^{(2N+1)}$ (absorptive nonlinearity) depend simultaneously on the real and imaginary parts of the NP susceptibilities. Notice that by adjusting the value of $f$ it is possible to cancel either $\text{Re}\chi_{\text{eff}}^{(3)}$ or $\text{Im}\chi_{\text{eff}}^{(3)}$, as first demonstrated in [101], but in either case the other nonlinearities are not necessarily suppressed.

Moreover, as will be shown in Section 5, by adjusting $f$ and the laser intensity it is possible to cancel the contribution of two nonlinearities leaving not null the third one.

## 5. NONLINEARITY MANAGEMENT PROCEDURE TO EXPLOIT HIGH-ORDER NONLINEARITIES

*Nonlinearity management* procedures in nonlinear optics appeared as a strategy to achieve stable propagation of intense optical beams in layered Kerr media [102]. The collapse arrest of $[(2+1)\mathrm{D}]$ two-dimensional soliton in Kerr-type optical media [102,103], as well as in Bose–Einstein condensate [104], were among the various motivations to develop *nonlinearity management* procedures.

When applied to the study of MDNCs, the *nonlinearity management* can be done by varying $f$ and the incident laser intensity [98,105]. Indeed, due to large nonlinearity of metallic NPs, small changes in the filling fraction may produce significant modifications of the effective NL response of the nanocomposite [72,101,106,107]. Remarkable is the observation that when the metallic NPs and the host have NL susceptibilities with opposite signs, it is possible to increase, decrease, and even suppress the effective NL response of MDNCs by adjusting the values of $f$ and $I$ [98,101,105].

Since metallic NPs exhibit relevant HON [67,80,81], interesting cases were reported with silver nanocolloids behaving as exotic materials with unique NL properties. For instance, nanocolloids consisting of spherical silver NPs (average diameter ~9 nm) suspended in acetone exhibit large third- and fifth-order contributions, when excited by the second harmonic of a $Q$-switched and mode-locked Nd:YAG laser (80 ps, 532 nm) for peak intensities in the range of 1–10 $\mathrm{GW/cm^2}$ [105]. Single pulses (selected using a pulse-picker), operating at low repetition rates (5–10 Hz), were used in all experiments described in this section, in order to prevent cumulative effects due to the thermal nonlinearity.

The NL characterization of silver nanocolloids, for different volume fractions of silver NPs, was reported in [98,105] by using the well-established Z-scan technique [64]. By applying that technique the effective NL refractive indices were obtained by measuring the transmitted beam intensity, through a small aperture placed in front of a photodetector in the far field [*closed-aperture* (CA) scheme], of a sample moving along the beam propagation direction ($Z$-axis) in the region where the laser beam is focused. Similarly, measurements of the effective NL absorption coefficients were performed by capture of all the light transmitted by the sample when the small aperture is removed [*open-aperture* (OA) scheme]. All measurements were calibrated by using liquid carbon disulfide ($\mathrm{CS_2}$), whose NL refractive index at 532 nm is known for moderate intensities ($n_2^{\mathrm{eff}} = +3.1 \times 10^{-14}\ \mathrm{cm^2/W}$) [108].

An extension of the Gaussian decomposition method [64] used to analyze the Z-scan curves, was presented in [67] to obtain expressions for the normalized CA and OA transmittances at the far field, given by

$$\text{CA scheme}: T(z, \Delta\Phi_{\mathrm{NL}}) \cong 1 + \sum_{N=1} \frac{(4N)\Delta\Phi_0^{(2N+1)}(z/z_0)}{[(z/z_0)^2 + (2N+1)^2][(z/z_0)^2 + 1]^N}, \tag{14}$$

$$\text{OA scheme}: T(z, q_0) \cong \frac{1}{\sqrt{\pi} q_0} \int_{-\infty}^{\infty} \ln[1 + q_0 \exp(-\tau^2)]\mathrm{d}\tau, \tag{15}$$

where the induced NL phase variation ($\Delta\Phi_{\mathrm{NL}}$) corresponds to the sum of the $(2N+1)$ th-order phase shift, $\Delta\Phi_{\mathrm{NL}} = \sum_{N=1} \Delta\Phi_0^{(2N+1)}$ with $\Delta\Phi_0^{(2N+1)} = k n_{2N}^{\mathrm{eff}} I^N L_{\mathrm{eff}}^{(N)}$, and $q_0 = \alpha_{\mathrm{NL}} I L_{\mathrm{eff}}^{(1)} [1 + (z/z_0)^2]^{-1}$ with $\alpha_{\mathrm{NL}} = \sum_N \alpha_{2N}^{\mathrm{eff}} I^N$. $I$ is the incident intensity,

$L_{\mathrm{eff}}^{(N)} = [1 - \exp(-N\alpha_0 L)]/[N\alpha_0]$ is the effective length of the medium, $L$ is the sample thickness, $k = 2\pi n_0/\lambda$, $\lambda$ is the laser wavelength, $z_0$ is the Rayleigh length of the focused beam, $n_{2N}^{\mathrm{eff}}$ and $\alpha_{2N}^{\mathrm{eff}}$ are the effective $(2N+1)$th- order refractive index and effective $(2N+1)$th-order absorption coefficient, respectively. However, to determine the effective NL coefficients there are a large number of parameters that must be fitted to the experimental results leading to significant errors. Then, in order to improve the fit procedure, a better way is to express the peak-valley transmittance variation, $\Delta T_{p,v}$, as a function of the incident intensity of the form [67]

$$\text{CA scheme}: \frac{\Delta T_{p,v}}{I} \cong 0.406 k n_2^{\mathrm{eff}} L_{\mathrm{eff}}^{(1)} + 0.210 k n_4^{\mathrm{eff}} I L_{\mathrm{eff}}^{(2)} + 0.130 k n_6^{\mathrm{eff}} I^2 L_{\mathrm{eff}}^{(3)} + \ldots, \tag{16}$$

$$\text{OA scheme}: \frac{\Delta T_{p,v}}{I} \cong (2)^{-\frac{3}{2}} L_{\mathrm{eff}}^{(1)} (\alpha_2^{\mathrm{eff}} + \alpha_4^{\mathrm{eff}} I + \alpha_6^{\mathrm{eff}} I^2 + \ldots), \tag{17}$$

that reduce the number of terms to be fitted, through a polynomial function. Equations (16) and (17) reveal that the ratio $\Delta T_{p,v}/I$ as a function of $I$ will be constant in cubic media while it shows a linear dependence with the intensity in cubic–quintic media. When a medium exhibits higher nonlinearity than fifth-order, a polynomial dependence of $\Delta T_{p,v}/I$ as a function of the intensity is observed.

Therefore, a suitable procedure for obtaining the effective NL parameters is to measure the transmittance variation, $\Delta T_{p,v}$, from the experimental CA and OA Z-scan curves, plot a graphic of $\Delta T_{p,v}/I$ versus the intensity, and then fit them using Eqs. (16) and (17), respectively. Finally, these coefficients are used in Eqs. (14) and (15) to model the CA and OA Z-scan curves, corroborating the values previously found. This was the procedure followed to determine the high-order NL parameters in nanocolloids containing either silver nanospheres [67] or gold nanoshells [80].

### 5.1. Scope and Limitations of the Nonlinearity Management in Metal–Dielectric Nanocomposites

One of the objectives of the *nonlinearity management* procedure is the control of the effective NL susceptibilities contributing to the optical response of a system. The data presented in Fig. 7 illustrate how this goal can be reached by varying the incident intensity and the volume fraction of silver NPs suspended in acetone and $CS_2$.

Due to the opposite signs of $\mathrm{Re}\,\chi^{(3)}$ in acetone and silver NPs, the effective third-order refractive index, $n_2^{\mathrm{eff}} \propto \mathrm{Re}\,\chi_{\mathrm{eff}}^{(3)}$, may be canceled by adjusting $f$ and the result is independent of the laser intensity, as shown in Eq. (11). Nevertheless, for $I > 6\ \mathrm{GW/cm^2}$, the fifth-order NL contributions are very important, as shown in Fig. 7(a). Notice that for $f = 1.6 \times 10^{-5}$ we have $n_2 = 0$ and $n_4 = +3.2 \times 10^{-25}\ \mathrm{cm^4/W^2}$.

The *nonlinearity management* can be useful also to control the absorptive response of the nanocomposites. For example, silver nanocolloids display a saturated absorption behavior when the laser frequency $\omega$ is near-resonance with $\omega_{\mathrm{LSP}}$. The linear dependence of effective third- and fifth-order absorption coefficients ($\alpha_2^{\mathrm{eff}} \propto \mathrm{Im}\,\chi_{\mathrm{eff}}^{(3)}$ and $\alpha_4^{\mathrm{eff}} \propto \mathrm{Im}\,\chi_{\mathrm{eff}}^{(5)}$) with $f$ can be observed in Fig. 7(b). However, no sign reversal of $\alpha_2^{\mathrm{eff}}$ was observed because the NL absorption coefficient of the host (acetone) is negligible for the experimental conditions considered here.

The *nonlinearity management* procedure was also applied to silver NPs (average diameter: ~6 nm) suspended in $CS_2$. In this case, because the silver NPs are smaller than in the previous case, the NL susceptibilities are larger [109] allowing the observation of the seventh-order susceptibility contribution [98]. Figure 7(c) shows that for $f = 3.3 \times 10^{-5}$ and $I = 0.1$ GW/cm$^2$, it is obtained a defocusing septimal medium $n_6^{\text{eff}} = -1.1 \times 10^{-30}$ cm$^6$/W$^3$, due to destructive interference between the third- and fifth-order susceptibilities. On the other hand, destructive interference between $n_2^{\text{eff}} \propto \text{Re}\chi_{\text{eff}}^{(3)}$ and $n_6^{\text{eff}} \propto \text{Re}\chi_{\text{eff}}^{(7)}$ in a nanocolloid with $f = 1.5 \times 10^{-5}$ produces a focusing quintic medium with $n_4^{\text{eff}} = +1.1 \times 10^{-22}$ cm$^4$/W$^2$, as shown in Fig. 7(d). In addition, management of the NL absorption coefficients can be performed by varying $f$ and controlling the incident intensity, as shown in Fig. 7(e). In particular, for $f = 1.2 \times 10^{-5}$ and $I = 0.25$ GW/cm$^2$, it is obtained an absorptive septimal medium with $\alpha_6^{\text{eff}} = -7.5 \times 10^{-27}$ cm$^5$/W$^3$.

Therefore, the *nonlinearity management* procedure presented here is a simple, but efficient, methodology to control the optical response of a MDNC in order to obtain

Figure 7

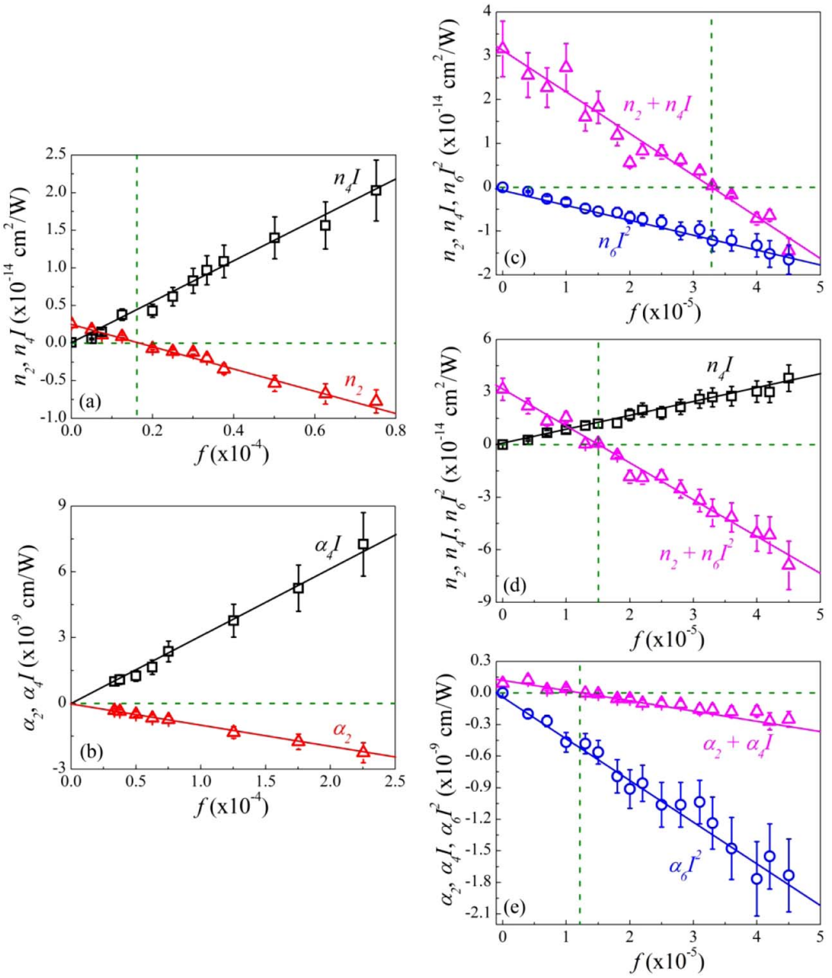

Dependence of the effective NL parameters as a function of the volume fraction, $f$. For silver NPs suspended in acetone: (a) $n_2^{\text{eff}}$ and $n_4^{\text{eff}}I$ (focusing quintic medium with $f = 1.6 \times 10^{-5}$); (b) $\alpha_2^{\text{eff}}$ and $\alpha_4^{\text{eff}}I$ with $I = 9$ GW/cm$^2$. Adapted figure with permission from [105]. Copyright 2014 by the American Physical Society. For silver NPs suspended in CS$_2$: (c) $n_2^{\text{eff}} + n_4^{\text{eff}}I$ and $n_6^{\text{eff}}I^2$ (defocusing septimal medium with $f = 3.3 \times 10^{-5}$); (d) $n_2^{\text{eff}} + n_6^{\text{eff}}I^2$ and $n_4^{\text{eff}}I$ (focusing quintic medium with $f = 1.5 \times 10^{-5}$) with $I = 0.1$ GW/cm$^2$; (e) $\alpha_2^{\text{eff}} + \alpha_4^{\text{eff}}I$ and $\alpha_6^{\text{eff}}I^2$ (absorptive septimal medium with $f = 1.2 \times 10^{-5}$) with $I = 0.25$ GW/cm$^2$. Adapted with permission from [98].

appropriate conditions to study particular high-order phenomena. Although the conditions to increase, decrease, or eliminate specific NL refractive indices or NL absorption coefficients were identified, an easier control of both coefficients may be achieved dealing with multicomponent MDNCs, although such applications were not reported yet.

Finally, we emphasize that in all experiments considered here the validity conditions of the Maxwell–Garnet model were obeyed, that is, the particles size was smaller than their separation distance, which is also considerably smaller than the wavelength used, leading to very small volumetric fractions ($f \ll 1$). Studies of MDNCs having larger values of $f$ would require approaches based on other effective models mentioned in Section 4. It is important to mention that for larger NP densities, phenomena not considered here, such as tunneling, clustering, and multiple light scattering, may play an important role affecting the NL behavior of the MDNCs. In particular, for some specific large values of $f$ and appropriate NP sizes, one may find very large local field amplitudes, inter-NP interactions, and efficient scattering of light that may lead to optical behaviors related to a variety of phenomena and possible applications, such as localization of light [110], coherent energy transport along NP arrays [111], and light trapping [112,113]. In such cases the Maxwell–Garnet model and the *nonlinearity management* procedure herein presented cannot be applied.

## 6. APPLICATIONS OF THE NONLINEARITY MANAGEMENT PROCEDURE

This section illustrates how the *nonlinearity management* procedure can be used to investigate effects due to HON under different experimental conditions. In the spatial regime we review the effects of self- and cross-phase modulation, modulation instability, and soliton propagation. In the temporal regime we analyze the electric field polarization instability of a laser beam propagating in a silver nanocolloid. The experimental results illustrate how to use the *nonlinearity management* to compensate the diffraction (dispersion), in the spatial (temporal) regime, by selecting the appropriate values of $f$ and $I$. Finally, the *nonlinearity management* procedure is applied to show how to optimize all-optical switches.

### 6.1. Spatial Self-Phase Modulation

The interaction of an intense coherent beam with a medium that presents an intensity-dependent refractive index produces changes in the beam phase that are manifested on the transverse beam profile [8,114]. This effect, known as spatial self-phase modulation (SSPM), generates a concentric ring intensity pattern observed in the far field [Fig. 8(a)]. The first observation of SSPM was reported in $CS_2$, illuminated by a He–Ne laser, due to refractive index modulation induced by thermal effects [115]. Subsequently, several studies were reported in media exhibiting thermal nonlinearities [116–123], Kerr-type media [124–127], photorefractive crystals [128], nematic liquid crystals [129–131], and a variety of other physical systems [132–136]. The SSPM effect in MDNCs has been studied by several authors [121–126] but only low-order nonlinearities were investigated.

An experimental report on SSPM induced in a MDNC with NL response dominated by the quintic nonlinearity was published in [98]. The MDNC used was a silver nanocolloid with $f = 1.6 \times 10^{-5}$ that, according to Fig. 7(a), is a focusing quintic NL medium ($n_4^{\mathrm{eff}} > 0$) with suppressed refractive cubic nonlinearity ($n_2^{\mathrm{eff}} = 0$). The far-field diffraction patterns were produced by focusing a Gaussian laser beam 532) nm, pulse duration: 80 ps, 10 Hz, beam waist: 7 μm) on the input face of a glass cuvette (thickness: 1 mm) containing silver NPs in acetone, as indicated in Fig. 8(a). The dependence of the intensity patterns with the wavefront curvature radius (R) was analyzed by locating the sample (S) in three positions: the focal plane of the lens L where $R \to \infty$, 0.3 mm before ($R < 0$), and 0.3 mm after ($R > 0$) the focal plane.

Figures 8(b)–8(d) show the diffraction patterns in the far field (20 cm from the exit plane of the sample) for intensities of 70, 90, and 100 $\mathrm{GW/cm^2}$, when the sample is located in the focal point. Because of the intensity dependence of the NL phase shift, the diffraction patterns consist of concentric rings that vary in number, thickness, and separation distance with the laser intensity. It is observed that higher intensities, corresponding to larger NL phase shift induced by HON, produce larger number of rings in the far field. Therefore, the SSPM effect is enhanced because the HON contributions depend on the high powers of the incident electric field ($I^N \propto |E|^{2N}, N = 1, 2, 3, \ldots$). Figures 8(e) and 8(f) show the intensity patterns, in the far field, for the same intensity as Fig. 8(b) ($I = 70\ \mathrm{GW/cm^2}$), but with the sample located before ($R < 0$) and after ($R > 0$) the focal point, respectively. The diffraction patterns depend on the sign of the product between the wavefront curvature radius and the NL phase shift as it was predicted for cubic media [137].

Calculations based on the Fraunhofer approximation of the Fresnel–Kirchhoff diffraction integral were made to reproduce the SSPM patterns. The intensity distribution in the far field was modeled by

$$I = I_0 \left| \int_0^{\infty} J_0(k\theta r) \exp\left[ -\frac{r^2}{w_{\mathrm{in}}^2} - i\phi(r) \right] r\mathrm{d}r \right|^2, \tag{18}$$

where $I_0 = 4\pi^2 |E(0, z_0) \exp[-\alpha_0 L/2]/(i\lambda D)|$, $E(0, z_0)$ is the electric field at the beam axis, $z_0$ is the focal plane position, $r$ is the radial distance from the laser axis, $\theta$ is the far-field diffraction angle, and $J_0(k\theta r)$ is the first-kind zero-order Bessel function. The total phase-shift, $\phi(r) = kn_0 r^2/(2R) + \Delta\Phi_{\mathrm{NL}} \exp(-2r^2/w_{\mathrm{in}}^2)$, includes the Gaussian phase due to the linear propagation plus the NL phase shift,

Figure 8

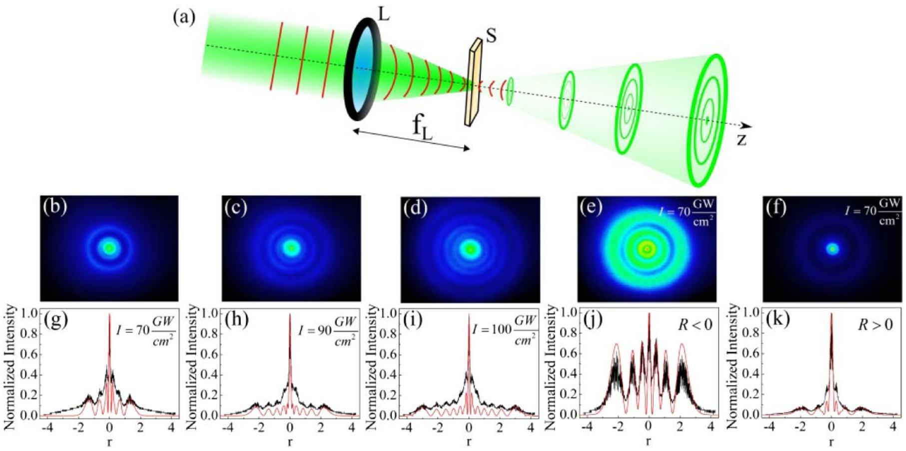

(a) Experimental setup of SSPM effect: lens (L) with focal distance ($f_L = 20$ mm) focusing a laser beam on a NL sample (S). (b) Far-field diffraction patterns produced by the MDNC, with NL response dominated by the quintic nonlinearity, placed in (b)–(d) the focal plane and (e) before and (f) after the focal plane. Laser peak intensities of (b),(e),(f) 70 $\mathrm{GW/cm^2}$, (c) 90 $\mathrm{GW/cm^2}$, and (d) 100 $\mathrm{GW/cm^2}$. (g)–(k) Experimental intensity distributions (black lines) corresponding to (b)–(f), respectively. Red lines show the numerical simulations obtained from Eq. (18), using the NL coefficients obtained by Z-scan technique. Adapted with permission from [98].

$\Delta\Phi_{\mathrm{NL}} = \sum_{N=1} k n_{2N}^{\mathrm{eff}} I^N [1 - \exp(-N\alpha_0 L)]/N\alpha_0$. The parameter $w_{\mathrm{in}}$ is the beam radius at the entrance plane of the sample and $D$ is the distance from the exit plane of the cell to the detection plane.

The black lines in Figs. 8(g)–8(k) display the intensity distributions obtained from Figs. 8(b)–8(f), respectively; the red lines correspond to the numerical results obtained from Eq. (18), with the NL coefficients obtained by the Z-scan technique (Fig. 7), showing that the number of rings, their thickness and spacing are in good agreement with the numerical results. However, the experimental results exhibit a low-intensity background produced by linear light scattering.

### 6.2. Spatial Modulation Instability

Spatial modulation instability (SMI) is a phenomenon that appears due to competition between nonlinearity and diffraction effects being enhanced by the exponential growth of the optical field amplitude and phase noise [110]. The SMI may be strongly affected by high-order dispersive effects [138,139], saturation of the nonlinearity [140], nonlocal nonlinearity [141,142], and coherence properties of optical beams [143,144]. The instability growth produces changes in the transverse beam profile, along the light beam propagation, which may lead to a filamentation regime [145].

The study of SMI induced by XPM involving HON was investigated in various theoretical works [146–149] but it was demonstrated only recently [98,105] thanks to the *nonlinearity management* of the silver nanocolloids. For this purpose, experiments were performed to analyze the response of the MDNCs managed to present cubic, quintic, and septimal nonlinearities. The pump and probe Gaussian beams with an intensity ratio of 10:1 were aligned to counter-propagate along a sample having a thickness of 5 cm. Temporal and spatial overlap of the laser pulses were adjusted carefully and constantly monitored. Figure 9 illustrates the XPM transverse SMI for three volume filling fractions of silver NPs suspended in acetone. Because the pump beam intensity is 2 GW/cm$^2$, the three columns of Fig. 9 correspond to a refractive cubic medium ($f = 0.5 \times 10^{-5}$), refractive quintic medium ($f = 1.6 \times 10^{-5}$), and cubic–quintic medium ($f = 2.5 \times 10^{-5}$), respectively. Figures 9(a)–9(c) display the probe beam transverse profiles, after propagation through the MDNCs, in the presence of the pump beam. In these images it is possible to appreciate two characteristic SMI features. The first one is the difference in the three beams spot size, which is understood because the contributions of cubic and quintic nonlinearities have opposite signs. The second feature refers to the formation of new spatial frequencies induced by the SMI effect that can be identified by the intensity decrease in the center of the probe beam profile.

Figures 9(d)–9(f) show the probe beam intensity profiles corresponding to Figs. 9(a)–9(c), versus the normalized radial coordinate. It is possible to observe that the SMI effect is enhanced in the quintic medium [Fig. 9(e)] and in the medium exhibiting third- and fifth-order NL contributions [Fig. 9(f)]. Figures 9(g)–9(i) show the result of numerical simulations based on two-coupled NL Schrödinger equations (NLSEs) considering the contributions of HON, for each sample, as described below [Eq. (19)]. It can be seen that there is an excellent agreement between the experimental and numerical results.

Another experiment was reported with silver NPs suspended in CS$_2$, in order to study the SMI induced by XPM in a MDNC with dominant defocusing septimal nonlinearity [98]. In this case the spatial transverse overlap between the pump and probe beams was varied in a controlled way and changes in the probe beam profile can be observed. To fabricate a refractive septimal medium the metal nanocolloid was prepared with $f = 3.3 \times 10^{-5}$ and the pump beam intensity was 0.1 GW/cm$^2$.

Figures 10(a)–10(c) show the probe beam profile distortions produced by XPM for different relative distances between the beams' centers. The relative positions of the beams can be identified in Figs. 10(a)–10(c), where the pump and probe beams are represented by the white and pink lines, respectively. The black lines in Figs. 10(d)–10(f) correspond to the intensity profiles of the probe beam in the presence of the pump beam, obtained from Figs. 10(a)–10(c). The dashed red lines represent the output probe beam profiles in the absence of the pump beam, i.e., the probe beam being affected only by the linear diffraction. Figures 10(a) and 10(d), corresponding to the optimum spatial overlap of the beams, show the generation of new spatial frequencies as in Fig. 9(b), but induced by the septimal effective nonlinearity. A clear focusing of the probe beam induced by the pump beam is observed in Fig. 10(e), although the sample is a defocusing medium ($n_6^{\mathrm{eff}} < 0$). This behavior is analogous to the third-order effect predicted in [150] and observed in a defocusing cubic medium [151].

The output beams' profiles were described by modeling the light propagation of the probe and pump beams using the two-coupled equations considering the NL contributions up to the seventh order, given by

$$(-1)^j 2ik\frac{\partial E_j}{\partial z} + \Delta E_j = -\frac{\omega^2}{c^2}\left\{\begin{array}{l} 3\chi_{\mathrm{eff}}^{(3)}[2(|E_1|^2+|E_2|^2)-|E_j|^2] \\ +10\chi_{\mathrm{eff}}^{(5)}[3(|E_1|^2+|E_2|^2)^2-2|E_j|^4] \\ +35\chi_{\mathrm{eff}}^{(7)}[4(|E_1|^2+|E_2|^2)^3+3|E_j|^2[2(|E_1|^4+|E_2|^4)-3|E_j|^4]] \end{array}\right\}E_j, \qquad (19)$$

Figure 9

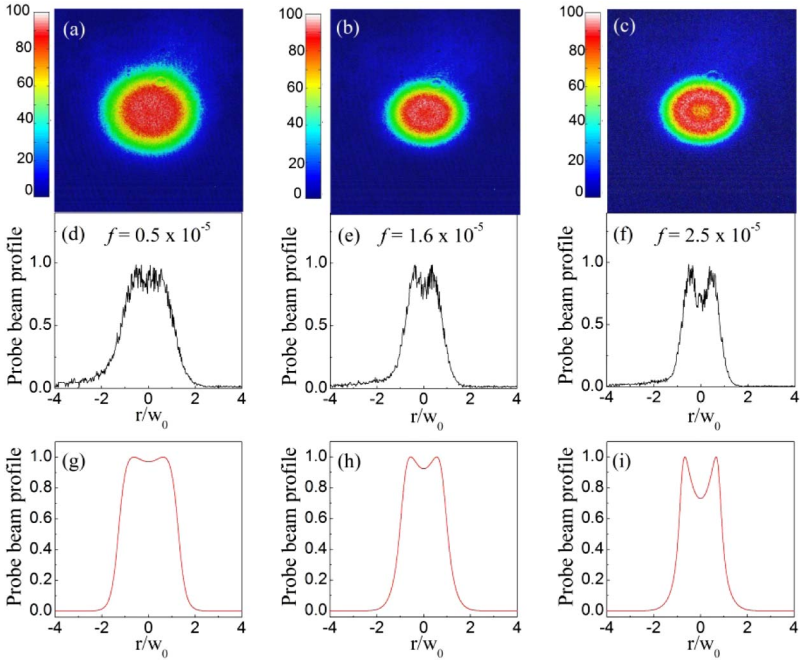

Transverse profile of the probe beam due to XPM-induced transverse SMI in (a) cubic, (b) quintic, and (c) cubic–quintic media. (d)–(f) Normalized intensity distributions versus normalized radial coordinate obtained from (a)–(c), respectively. (g)–(i) Numerical results obtained from Eq. (19) using the susceptibility values from Figs. 7(a) and 7(b). Pump beam intensity: 2 $\mathrm{GW/cm^2}$; probe beam intensity: 0.2 $\mathrm{GW/cm^2}$. Reprinted with permission from [105]. Copyright 2014 by the American Physical Society.

with $j = 1, 2$. $E_1$ and $E_2$ are the field amplitudes of the pump and probe beams, respectively. $\Delta$ is the transverse Laplacian operator, $\omega$ is the laser frequency, and $c$ is the speed of light in vacuum. The susceptibility values were obtained from Fig. 7, considering $\chi^{(3)}_{\mathrm{eff}} = 2\varepsilon_0 n_0^2 c/3(2n_2^{\mathrm{eff}} + i\alpha_2^{\mathrm{eff}} c/\omega)$, $\chi^{(5)}_{\mathrm{eff}} = 2\varepsilon_0^2 n_0^3 c^2/5(2n_4^{\mathrm{eff}} + i\alpha_4^{\mathrm{eff}} c/\omega)$, and $\chi^{(7)}_{\mathrm{eff}} = 8\varepsilon_0^3 n_0^4 c^3/35(2n_6^{\mathrm{eff}} + i\alpha_6^{\mathrm{eff}} c/\omega)$ [67], where $\varepsilon_0$ is the permittivity of free-space.

Since analytical solutions of the NLSE are known only for a few cases—the properties of solutions are normally investigated by numerical methods—in order to understand the dynamics of pulse propagation, perturbation theory was adopted to understand most of the phenomena described in this review. Another way that may offer accurate solutions is the Volterra series transfer function (VSTF) approach [152], which is generally used to model the pulse propagation through optical fibers in the frequency domain, including contributions of cubic nonlinearities. Nevertheless, its complex analytical form and its divergence analysis not only make its physical interpretation difficult, but also less attractive in terms of computational time compared to the well-known split-step Fourier method. To our knowledge, solutions of NLSEs with contributions of HON using the VSTF approach have not been reported in the literature yet.

Figures 10(g)–10(i) show the intensity distributions of the probe beam, obtained by numerical solutions of Eq. (19) using $n_2^{\mathrm{eff}} = n_4^{\mathrm{eff}} = 0$ and $n_6^{\mathrm{eff}} = -1.1 \times 10^{-30}\ \mathrm{cm}^6/\mathrm{W}^3$. The numerical simulations corroborate that the experimentally observed SMI effects are due to the seventh-order NL contributions.

Figure 10

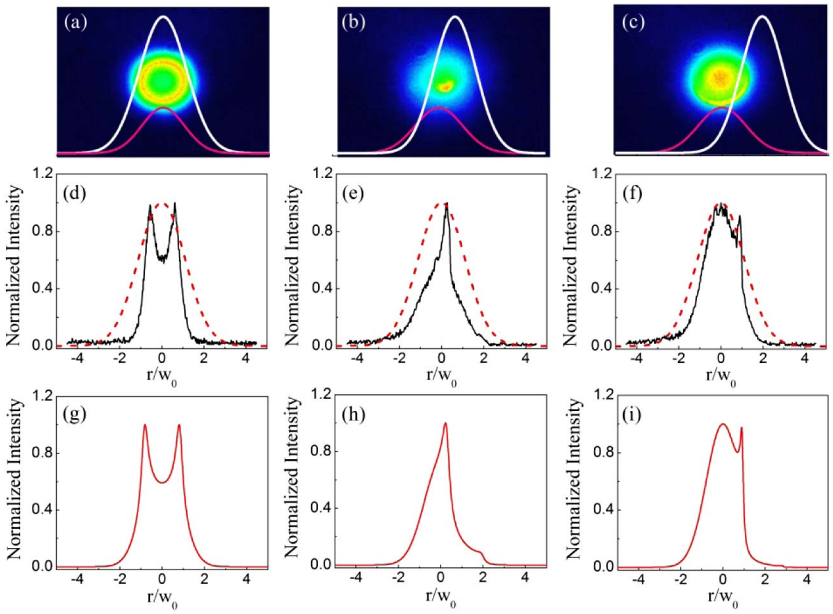

Transverse profile of the probe beam, due to XPM-induced transverse SMI in a septimal medium, for beams separation of (a) 0, (b) $w_0$, and (c) $2.2w_0$, between the centers of the incident pump (white line) and probe (pink line) beams, where $w_0$ is the beam waist. (d)–(f) Normalized intensity distributions of the probe beam in the presence (black lines) and absence (red lines) of the pump beam, obtained from (a)–(c), respectively. (g)–(i) Numerical results obtained from Eq. (19) using $n_2^{\mathrm{eff}} = n_4^{\mathrm{eff}} = 0$ and $n_6^{\mathrm{eff}} = -1.1 \times 10^{-30}\ \mathrm{cm}^6/\mathrm{W}^3$. Pump beam intensity: 0.1 GW/cm$^2$; probe beam intensity: 0.01 GW/cm$^2$. Reprinted with permission from [98].

Therefore, the experimental and numerical results of Figs. 9 and 10 illustrate the important contributions of HON to SMI. Of course tracking down these results was possible thanks to the application of the *nonlinearity management* procedure, which allows the discrimination among the different NL order contributions.

Other applications of the *nonlinearity management* are extremely attractive since the SMI effect has important connections with various NL processes. A particular example is the stable propagation of spatial solitons, which will be discussed in Subsection 6.3. One relation between SMI and spatial solitons is manifested in the fact that the filaments that emerge from the SMI process have the behavior of solitary waves that under certain conditions may travel without suffering deformation [142].

### 6.3. Bright and Vortex Solitons

Optical spatial solitons are self-trapped light beams that remain with their shape and transverse dimension invariant along propagation, due to the balance between diffraction and NL interaction [153–156]. Nowadays, several families of spatial solitons supported by different types of nonlinearities are theoretically and experimentally recognized [156]. In this section we will focus our attention on the study of the spatial solitons propagation in silver nanocolloids.

In self-focusing media, spatial bright solitons (SBSs) are stable in one transverse dimension [$(1+1)$D] and their propagation is modeled by the cubic NLSE, resulting in a commonly known hyperbolic-secant shaped beam [157,158]. On the contrary, in two transverse dimensions [$(2+1)$D], SBSs are not stable when only the instantaneous cubic nonlinearity is present and catastrophic collapse is observed [159–161]. However, several works show alternative methods to arrest the beam collapse, such as considering saturation of the nonlinearity [162], the presence of HON [163,164], nonlocal nonlinearity [165], and inclusion of dissipative terms [166,167]. Our special interest in this section is the stable propagation of $(2+1)$D SBSs in MDNCs exhibiting HON. Therefore the experiment described below was inspired by recent experiments: (*i*) the observation of robust $(2+1)$D SBS propagation in liquid $CS_2$ due to the simultaneous contributions of focusing cubic and defocusing quintic nonlinearities [168]; and (*ii*) four-wave mixing experiments, based on the competition of cubic and quintic nonlinearities, performed to demonstrate the stabilization, for long distances, of $(2+1)$D SBS in a rarefied gas [169] and in a nonresonant Kerr glass [170]. Notice that SBS could not propagate in the silver nanocolloids exhibiting cubic–quintic nonlinearities because the NL response would be dominated by the defocusing cubic nonlinearity. Nevertheless, the *nonlinearity management* procedure allows the fabrication of a silver nanocolloid presenting effective quintic–septimal (focusing–defocusing) refractive nonlinearities with suppressed cubic refractive nonlinearity. Therefore, the stable propagation of $(2+1)$D SBSs, for ~10 Rayleigh lengths, became possible, as reported in [171]. Figure 11(a) displays the experimental setup used that consisted of a pulsed laser (80 ps; 532 nm), with transverse Gaussian profile, focused at the input face of the sample with a beam waist of ~7 μm. The beam propagation along the sample was recorded by two CCD cameras placed on the laser beam axis and in the direction perpendicular to the beam axis. For the analysis of the images collected in the transverse direction the scattered light imaging method (SLIM) [172,173] was used.

Figure 11(b) displays the behavior of the output beam radius as a function of the incident intensity, after the beam passed through a 2 mm long cell (~8 Rayleigh lengths), containing the quintic–septimal medium. The results show that for low intensities the beam diverges rapidly due to the linear diffraction. However, the beam divergence decreases when the intensity is increased, until reaching a minimum beam radius of 7 μm, for $I \geq 60\ \mathrm{GW/cm^2}$, that corresponds to the beam waist at the entrance face of the cell. That is, the beam propagates without deformation along the sample. Such interpretation was confirmed by analyzing the beam side-view images, shown in Fig. 11(c). For $I > 20\ \mathrm{GW/cm^2}$, it is possible to observe regions where the beam radius remains constant. The maximum propagation distance of ~2.3 mm with constant beam radius was observed for $I \geq 70\ \mathrm{GW/cm^2}$. Numerical simulations based on the quintic–septimal NLSE [Fig. 11(d)] were performed considering the intensities used in the experiments ($7\ \mathrm{GW/cm^2} \leq I \leq 85\ \mathrm{GW/cm^2}$) and using the NL susceptibilities corresponding to $f = 1.6 \times 10^{-5}$ according to the results displayed in Figs. 7(a) and 7(b) ($\chi_{\mathrm{eff}}^{(3)} = -i6.3 \times 10^{-22}\ \mathrm{m^2/V^2}$, $\chi_{\mathrm{eff}}^{(5)} = 3.7 \times 10^{-38} + i3.3 \times 10^{-37}\ \mathrm{m^4/V^4}$, and $\chi_{\mathrm{eff}}^{(7)} = -4.2 \times 10^{-54} - i3.5 \times 10^{-54}\ \mathrm{m^6/V^6}$). It should be noted that the seventh-order contributions for silver NPs in acetone are negligible for $I < 20\ \mathrm{GW/cm^2}$, and for this reason they do not appear explicit in Figs. 7(a) and 7(b).

Figures 11(e) and 11(f) show the evolution of the experimental and theoretical beam radius along the propagation, obtained from the side-view images of Figs. 11(c) and 11(d), respectively. The shaded rectangles display the regions of stable SBS propagation showing very good agreement between the experimental and theoretical results.

Therefore the results of Fig. 11 show a direct application of the *nonlinearity management* procedure aiming the stable propagation of (2 + 1)D SBSs, obtained by managing the silver nanocolloid to present a quintic–septimal (focusing–defocusing)

Figure 11

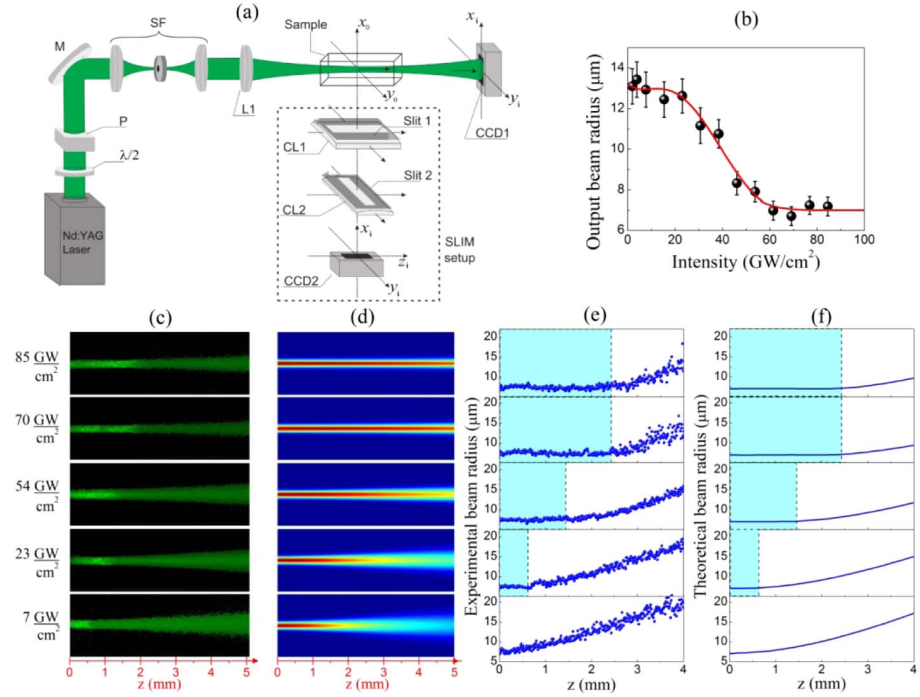

(a) Experimental setup for analysis of (2 + 1)D SBS in a quintic–septimal medium. (b) Dependence of the transmitted laser beam radius, after 2 mm long cell, as a function of the input intensity. (c) Experimental and (d) theoretical side-view images of the SBS propagation, for different intensities. (e) Experimental and (f) theoretical beam radius as a function of propagation distance obtained from (c) and (d), respectively. Adapted figure with permission from [171]. Copyright 2014 by the American Physical Society.

response with suppressed cubic refractive nonlinearity. These results corroborate the theoretical predictions of using HON to arrest the catastrophic self-focusing. Although in the present case the simultaneous contributions of HON enable to avoid the beam collapse in $(2 + 1)$D, one should be aware that under certain specific conditions HON contributions can produce critical [174] or supercritical beam collapse [175], even in $(1 + 1)$D.

On the other hand, self-defocusing media support the stable propagation of optical dark and vortex solitons [156,176,177]. Spatial dark solitons (SDSs) show an intensity dip with a phase jump across it, in the axis of an extended bright beam. Theoretically, $(1 + 1)$D SDS was first proposed as a solution to the exactly integrable NLSE equation with negative cubic nonlinearity [178]. The experimental observation of quasi-$(1 + 1)$D SDSs was reported in self-defocusing sodium vapor [179]. However, the $(2 + 1)$D SDSs are affected by the transverse SMI [180] leading to their bending and eventual decay into vortices [181].

Optical vortices are $(2 + 1)$D axisymmetric beams with a phase singularity and zero amplitude at the pivot, which carry a nonzero orbital angular momentum (OAM) [176,177,182]. A light beam carrying OAM has a phase in the transverse plane of $\theta(r, \phi) = \exp(il\phi)$, where $\phi$ is the angular coordinate and $l$ can be any integer, positive or negative. For a given $l$, the beam has $l$ intertwined phase fronts, as illustrated in Fig. 12; the handedness of the beam is determined by its sign.

A simple way to produce an OAM carrying beam is passing a Gaussian beam through a spiral phase plate—a piece of polymer with helical surface, as illustrated in Fig. 13. The optical thickness of the plate varies with the azimuthal coordinate according to $l\lambda\phi/[2\pi(n - 1)]$, where $n$ is the refractive index of the polymer. Shaped optical vortices with arbitrary spatial profile can be obtained using a liquid-crystals-based spatial light modulator [183].

In self-defocusing media, vortex beams can behave as optical vortex solitons (OVSs) when the diffraction effect is balanced by the defocusing nonlinearity [184,185]. In general, spatial solitons have large potential for applications in optical data storage, transmission, and data processing [156,176]. However, OVSs are highlight by their

Figure 12

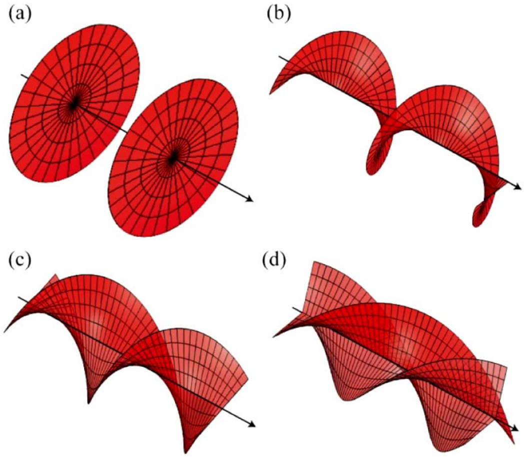

Representations of beams carrying optical angular momentum. The Poynting vector is not parallel to the propagation direction and follows a spiral trajectory around the beam axis. Helical phase fronts for (a) $l = 0$, (b) $l = 1$, (c) $l = 2$, and (d) $l = 3$. Reprinted with permission from [182]. Copyright 2011 Optical Society of America.

direct applications in the interaction of light with matter such as the OAM transfer [182]. Moreover, OVSs also contribute in applications based on the control of light-by-light. Due to their ring-like intensity profile, OVSs are used to induce waveguide in order to confine and guide light inside the vortex core [186,187].

Recently, an experimental demonstration of the stable OVS propagation was reported in a cubic–quintic medium by using the *nonlinearity management* procedure in a colloid consisting of silver NPs suspended in acetone [188]. A schematic of the experimental setup is shown in Fig. 14. The excitation (pump) beam was the second harmonic of a Nd:YAG laser (532 nm, 80 ps, 10 Hz, maximum pulse energy of 10 μJ) and the probe beam was obtained from a HeNe laser (632.8 nm, 10 mW). The optical vortex beam at 532 nm was produced using one spiral phase plate with $l = 1$. The vortex beam was focused by a lens on the input face of a cell containing the silver nanocolloid and a set of lenses was used to adjust the probe beam waist to be approximately equal to the vortex core radius. Cells with thicknesses of 3, 5, and 10 mm were used. A special scheme to synchronize the detected HeNe laser signal with the pump pulses was used, as described in [188].

Figure 13

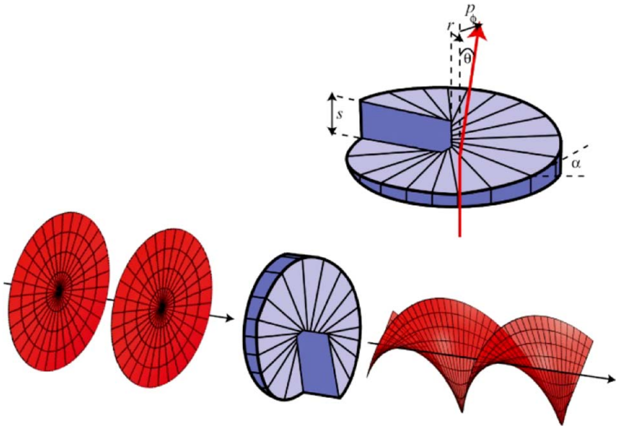

Spiral phase plate used to generate beams carrying optical angular momentum. Reprinted with permission from [182]. Copyright 2011 Optical Society of America.

Figure 14

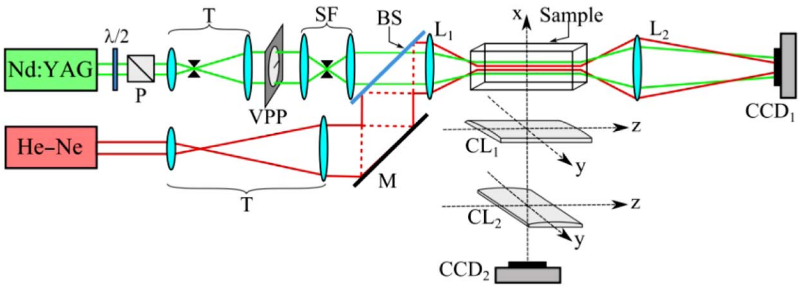

Experimental setup: P, polarizer; T, telescope; VPP, vortex phase plate; M, mirror; SF, spatial filter; BS, beam splitter; spherical lenses with $f_1 = 5$ mm (L$_1$) and $f_2 = 5$ mm (L$_2$). Camera CCD$_1$ produced the transmitted-beam spatial profile. Cylindrical lenses with $f = 40$ mm (CL$_1$) and $f = 80$ mm (CL$_2$), and CCD$_2$ were used in the SLIM setup. The cell's length is 10 mm. Reprinted with permission from [188].

The silver colloid was prepared in order to exhibit a dominant defocusing cubic nonlinearity with focusing quintic NL contribution by choosing $f = 3 \times 10^{-5}$, which corresponds to $\chi^{(3)}_{\text{eff}} = -(8.3 + i2.7) \times 10^{-21}\ \text{m}^2/\text{V}^2$ and $\chi^{(5)}_{\text{eff}} = (2.8 + i0.2) \times 10^{-35}\ \text{m}^4/\text{V}^4$, as in Figs. 7(a) and 7(b). Figure 15(a) shows the experimental transverse vortex beam images, for a propagation distance over 10 mm (~6 Rayleigh lengths), inside the cubic–quintic medium. Invariance of the shape and the external radius size of the vortex beam was observed for $I = 3\ \text{GW/cm}^2$. The vortex core presented a slight divergence in the beginning of the propagation and then remains constant, giving rise to the stable OVS propagation.

The stable OVS propagation illustrated by Fig. 15(a) is corroborated by the numerical calculations based on the cubic–quintic NLSE shown in Fig. 15(b). For low intensity ($I = 0.1\ \text{GW/cm}^2$) the vortex beam diverges due to the linear diffraction. However, for $I = 3\ \text{GW/cm}^2$ the stable propagation of OVSs over 10 mm is observed. Here, the simultaneous contributions of cubic and quintic nonlinearities are important to maintain both vortex core size and Gaussian background size invariant along the propagation [188].

Figure 15(c) shows the transverse beam profiles of the weak Gaussian beam being guided by the OVS illustrated by Fig. 15(a), with their respective intensity distributions. The Gaussian beam size in the entrance face of the cell was approximately equal to the vortex core size. With the simultaneous propagation of both beams, it is possible to observe that the central region of the Gaussian beam is guided by the OVS, along

Figure 15

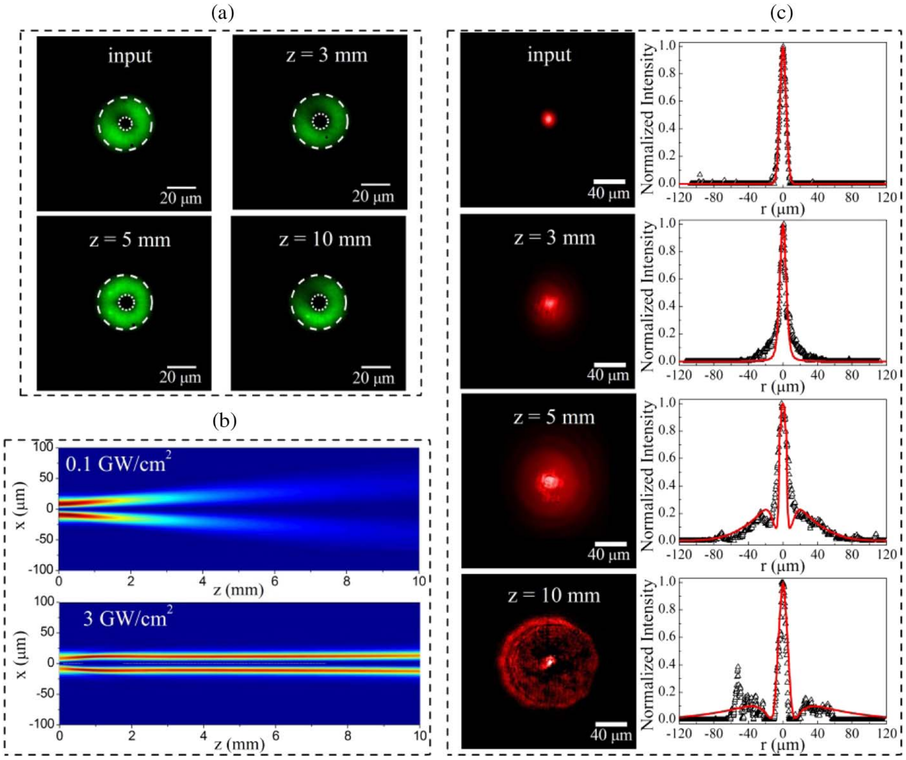

(a) Transverse vortex beam profiles behave as OVS, along 10 mm propagation distance. (b) Numerical simulation of the vortex beam propagation for intensities of $0.1\ \text{GW/cm}^2$ (linear behavior) and $3\ \text{GW/cm}^2$ (soliton-type behavior). (c) Transverse beam profiles and intensity distributions of a weak Gaussian beam being guided by the OVS described in (a). Adapted with permission from [188].

the 10 mm long cell. The light ring observed in the transverse beam profiles shown in Fig. 15(c) is due to an imperfect coupling of the Gaussian beam into the vortex core, and to the small refractive index difference induced between the core and the bright region of the OVS, but it can be further improved by a more appropriate choice of the beams' sizes. The propagation of both beams was modeled by using two coupled cubic–quintic NLSEs and the results are illustrated by the red lines in Fig. 15(c).

Hence, the proof-of-principle experiment of [188], summarized in Figs. 14 and 15, illustrates the possible application in fast dynamic circuitry based on spatial solitons, since the NPs present a fast NL response based on the excitation of electronic local nonlinearities.

### 6.4. Polarization Instability Due to High-Order Nonlinearities

The motivation for developing fibers based MDNCs is due to the possible use in devices such as all-optical switches, wavelength converters, optical parametric amplifiers, etc. (see, for example, [189]). In principle, ultrafast optical devices require a high NL material with ultrafast time response and a setup compatible with the silica-fiber-based optical communication systems.

The use of metal NPs in photonic devices will require the development of suitable solid-state hosts. MDNCs based on inorganic glasses and some special polymers may be appropriate materials for the majority of applications because they present high transparency, large durability, low cost, high chemical stability, and low sensibility to moisture. The requirement of higher NL materials is justified because the minimization of dispersive effects would be achieved in short pieces of fibers.

Trials to develop optical fibers based on silicate glasses and polymers incorporated either with silver or gold NPs were reported [190–193], but only third-order experiments were performed using such fibers. However, as shown below, the exploitation of the fifth-order nonlinearity may be helpful for all-optical switching operations.

The interaction of an intense laser beam with a NL medium can produces changes in its polarization state, induced by the intensity-dependent refractive index of the material. One of the main effects related to the intensity-dependent polarization state is the NL birefringence, which produces the optical polarization rotation along the propagation through the NL medium [194]. This phenomenon was evidenced for the first time in liquids exhibiting cubic nonlinearity when they were excited with intense elliptically polarized light [195]. Subsequently, the NL birefringence was reported for different systems [196–200] and new proposals, based on HON contributions, were reported [201,202]. Indeed the NL birefringence effect was widely studied in optical fibers, being caused by the NL coupling among the various electromagnetic propagation modes [194]. When the NL contributions are large, the NL birefringence contributes to the polarization instability of the light beam [203,204] that is manifested by an enhanced sensitivity of the output state of polarization to small changes in the input power and/or the input polarization. Although the NL birefringence phenomenon has been successfully exploited for operation of all-optical devices [185], the main limitation for further exploitation of the effect is the long propagation distance required for observation of induced changes in the polarization of the light field. In this sense the experimental work of [205] indicates that optical fibers with HON may generate large variations in the polarization state in short propagation distances.

Figure 16(a) shows the experimental setup for the studies of NL polarization coupling and polarization instabilities, induced by HON, in a hollow capillary (length: 9 cm) filled with silver NPs suspended in $CS_2$. In the experiment the linearly polarized laser beam passes through a $\lambda/2$ phase plate and a polarizer used to control the incident intensity. A second $\lambda/2$ plate allows the rotation of the optical field linear polarization by an azimuth angle $\theta$. Two microscope objectives couple the light at the entrance of the capillary and collimate the transmitted light, which is detected by two fast detectors to analyze the transmittance variations as a function of incident azimuthal angle and intensity. A polarizing beam splitter was used to separate the vertical (V) and horizontal (H) polarization components.

The self-induced polarization rotation due to the silver nanocolloid was observed, as illustrated in Fig. 16(b), which shows results for samples with three different NP volume fractions. Notice that the normalized transmittance changes as a function of the incident polarization azimuth angle and exhibits drastic changes for different intensities. For low intensities ($I \leq 6\ \mathrm{MW/cm^2}$) the samples behave as a linear isotropic medium. Consequently, the normalized transmittance corresponding to the V-polarization (black circles) and H-polarization (red squares) exhibits a $\cos^2\theta$ and $\sin^2\theta$ dependence, respectively. For moderate intensity ($24\ \mathrm{MW/cm^2} \leq I \leq 60\ \mathrm{MW/cm^2}$), values of $\theta$ where the transmittance varies rapidly are observed due to the NL contributions. It is possible to note that the modulation effects are stronger when the medium presents quintic NL contributions. For the intensities used, the septimal NL contributions are negligible.

Figure 16

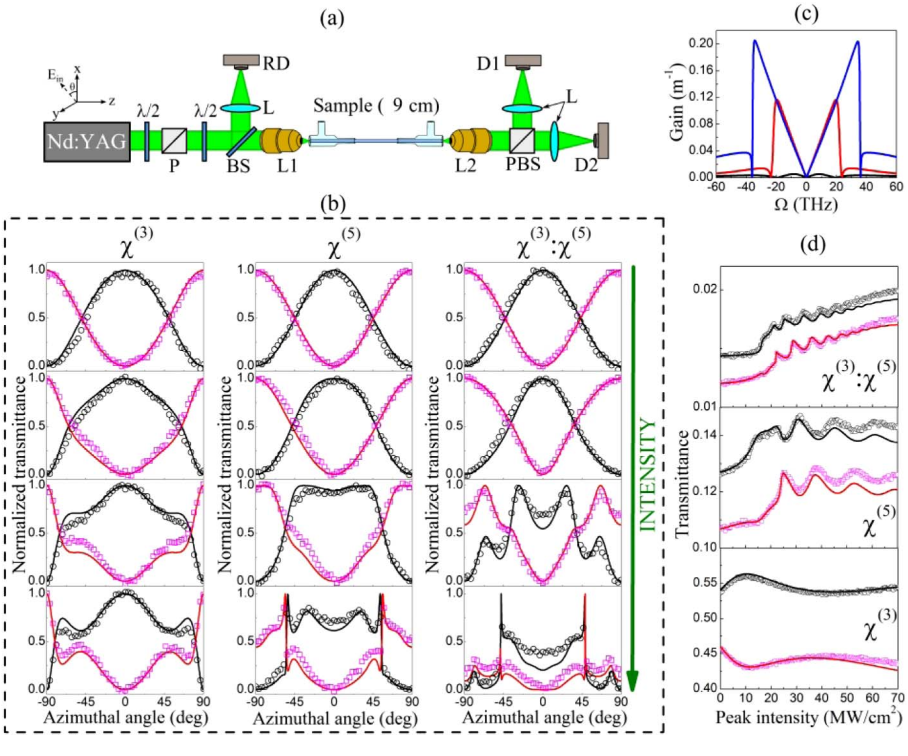

(a) Experimental setup for observation of the polarization instability effect. (b) Normalized transmittance as a function of the incident polarization azimuth angle for cubic, quintic, and cubic–quintic media. From top to bottom, the incident peak intensities are 6, 24, 42, and 60 $\mathrm{MW/cm^2}$. (c) Gain spectra of modulation instability versus the frequency shift along the fast axis cubic (black line), quintic (red line), and cubic–quintic (blue line) media. Incident intensity: 42 $\mathrm{MW/cm^2}$. (d) Vertical (black circles) and horizontal (red squares) polarization transmittance as a function of the incident peak intensities. Solid lines in (b) and (d) were obtained by numerical simulation of Eq. (20). Adapted with permission from [205].

The solid lines in Fig. 16(b) correspond to the numerical solutions of two coupled NL equations that describe the evolution of the right- ($A_+$) and left-circular polarization ($A_-$) along the capillary filled with either a cubic, quintic, or cubic–quintic isotropic medium. The equations describing the optical polarization are

$$\begin{aligned}&\frac{\partial A_\pm}{\partial z}+\frac{i}{2}\beta^{(2)}\frac{\partial^2 A_\pm}{\partial \tau^2}+\frac{\alpha_0}{2}A_\pm\\&=\frac{i}{2}(\Delta\beta_0)A_\mp+i\frac{\omega}{n_0c}F^{(1)}\chi^{(3)}_{xxxx}[(|A_+|^2+|A_-|^2)+|A_\mp|^2]A_\pm\\&\quad+i\frac{5\omega}{12n_0c}F^{(2)}\chi^{(5)}_{xxxxxx}\{4[|A_++A_-|^2(A_++A_-)^*\mp|A_+-A_-|^2(A_+-A_-)^*]A_\mp\\&\quad+[|A_++A_-|^4+|A_+-A_-|^4]\}A_\pm,\end{aligned}\tag{20}$$

where $n_0$, $\alpha_0$, $\beta^{(2)}$, and $\Delta\beta_0$ are the linear refractive index, linear absorption coefficient, second-order dispersion coefficient, and the modal birefringence of the capillary, respectively. $\omega$ is the laser frequency and $c$ is the speed of light in vacuum. The quantities represented by $F^{(j)}$, $j=1,2$, are $F^{(1)}=(\iint|F^{(0)}|^4\mathrm{d}x\mathrm{d}y)/(\iint|F^{(0)}|^2\mathrm{d}x\mathrm{d}y)^2$ and $F^{(2)}=(\iint|F^{(0)}|^6\mathrm{d}x\mathrm{d}y)/(\iint|F^{(0)}|^2\mathrm{d}x\mathrm{d}y)^3$, where $F^{(0)}$ is a fiber modal distribution, which was assumed as a Gaussian distribution for single-mode capillaries.

Figure 16(c) shows the gain spectra of the modulation instability induced by HON versus the frequency shift obtained by using a perturbation analysis on the Gaussian pulse amplitude in Eq. (20). The black line refers to a cubic medium with a very small fifth-order NL contribution corresponding to $f=10^{-5}$, as in Fig. 7(c). The red line refers to the quintic medium and the blue line is associated with a cubic–quintic medium and exhibits the relevant contribution of the effective fifth-order susceptibility. It is possible to identify that the growth rate of modulation instability is very much enhanced in the presence of the quintic nonlinearity. Distortions in the sidebands are attributed to linear losses [148].

The enhancement of the polarization instability effects can also be seen in media exhibiting only quintic nonlinearity, as shown in Fig. 16(d). Here, significant variations in the transmitted light intensity, corresponding to V- (black circles) and H-polarization (red squares), are observed for small changes in the incident intensity. The experimental results are corroborated by numerical simulations of Eq. (20), represented by the solid lines of Fig. 16(d).

In conclusion, we remark that large NL phase shift ($\sim 20\pi$) was observed in diluted silver nanocolloids with $f=10^{-5}$ showing that MDNC-based fibers or channel waveguides have very large potential for applications in all-optical switches.

### 6.5. All-Optical Switches Based on Metal–Dielectric Nanocomposites

The large growth of global communications requires data processing devices even faster than the ones already available. Then, all-optical devices for processing signals at bit rates of hundreds of GB/s up to TB/s are needed [206] and, for this reason, the identification of suitable NL materials is extremely important. Of course MDNCs are strong candidates due to their high NL refractive behavior and fast response, but the NL absorption may impair their application in devices such as AOSs. This problem is common of all materials with large nonlinearity, since normally large NL refractive index corresponds to large NL absorption coefficient [207]. Therefore, to identify suitable materials for AOSs, two figures of merit are considered: $T=|\alpha_2\lambda(n_2)^{-1}|$ and $W=|\Delta n(\alpha_0\lambda)^{-1}|$, where $\Delta n$ is the maximum variation of the refractive index that can be induced in the NL material, and to be useful the material have to present $T < 1$ and $W > 1$ [208,209].

Recently, the optimization of the figures of merit associated with MDNCs was reported with basis on the *nonlinearity management* procedure discussed in the previous sections [210]. Accordingly, since MDNCs present HON, one of the figures of merit should be redefined to be $T = |\alpha_{NL}\lambda(n_{NL})^{-1}|$, where $n_{NL} = n_2^{eff} + n_4^{eff}I + n_6^{eff}I^2$ and $\alpha_{NL} = \alpha_2^{eff} + \alpha_4^{eff}I + \alpha_6^{eff}I^2$. Therefore a systematic study of the figures of merit is presented in this section in a search for AOS optimization. The results obtained by studying silver nanocolloids with various NP volume filling fractions are illustrated in Fig. 17(a). For NL refraction, it is possible to observe that the value of $|n_{NL}|$ increases with increasing intensity. Nevertheless, for the NL absorption, $|\alpha_{NL}|$ is nullified for intensity of 8.6 GW/cm$^2$. This behavior was corroborated with the *open-aperture* Z-scan measurements [Fig. 17(b)], where a transmittance variation was not observed for $I = 8.6$ GW/cm$^2$. Cancellation of NL absorption is due to destructive interference between the imaginary parts of the third-, fifth-, and seventh-order susceptibilities. As a consequence, the ratio $T^{-1} \propto n_{NL}/\alpha_{NL}$ increases drastically, optimizing the figure of merit, shown in Fig. 17(c). The figure of merit $W$ is greater than 1 for intensities larger than 7 GW/cm$^2$. However, the value of $T$ was reduced by about 2 orders of magnitude for $I = 8.6$ GW/cm$^2$. Notice that it was plotted the values of $T^{-1}$ instead of $T$, i.e., $T^{-1} > 1$ is required for a suitable material to be used.

To certify the fast NL response of the MDNCs, a Kerr shutter experiment [79,211] was performed under the same conditions used in previous experiments. Figure 17(d) shows the Kerr shutter signal due to the fast NL response of the free electrons in the NPs. NL response time of tens of picoseconds was measured for silver colloids, being limited by the incident pulse duration of 80 ps. However, other experimental

Figure 17

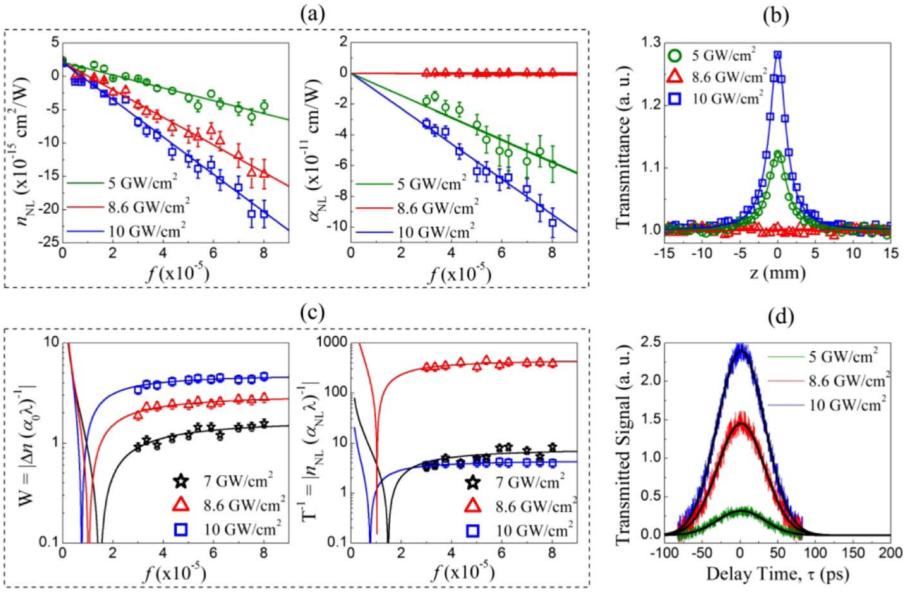

(a) Refractive and absorptive NL coefficients of silver colloids considering cubic, quintic, and septimal nonlinearities. (b) *Open-aperture* Z-scan profiles for silver colloids with $f = 5.9 \times 10^{-5}$. (c) Figures of merit ($W$ and $T^{-1}$) for AOS. (d) Kerr signals for silver colloids using a picosecond laser at 532 nm. Adapted with permission from [210].

work, carried out with shorter light pulses, reported NL response times of silver NPs of a few femtoseconds [212].

Therefore, the results shown in the Subsections 6.1–6.5 demonstrate that MDNCs are excellent materials for applications in ultrafast optical devices due to their fast response, high NL susceptibility, and the possibility of manipulating their NL response by changing the NP volume fraction and incident intensity.

## 7. FORESEEN ADVANCES IN THE STUDY OF HIGH-ORDER OPTICAL PHENOMENA

Many theoretical studies related to phenomena associated with HON can be found in the literature and the number of proposals is increasing due to the possible observation of new effects in MDNCs and analogies with atomic systems. Therefore, some theoretical and experimental results that can be considered for future experiments with MDNCs will be discussed in this section.

### 7.1. Stability Conditions for One-Dimensional Optical Solitons in Cubic–Quintic–Septimal Media

The stable propagation of spatial solitons, under various specific conditions, has been one of the topics of large interest in the past years. Usually the authors include in their models external potentials and look for stability conditions or assume that the medium of interest presents HON. For example, a special case studied from the theoretical point of view is the critical collapse in quintic media when the cubic nonlinearity is null. It was demonstrated that an external potential would allow arresting of the beam collapse in one-transverse dimension medium [213] and two-transverse dimension case [214]. When cubic–quintic media were considered it was shown that the cubic nonlinearity lifts the degeneracy of the Townes' solitons making their propagation stable [215]. Hence, a detailed study of soliton propagation in cubic–quintic–septimal media is important to complement the previous investigations and to foresee new research routes. In [175], the conditions for stable propagation of one-transverse dimension bright spatial solitons in media with HON up to the seventh-order was investigated. In this case the normalized cubic–quintic–septimal nonlinear Schrödinger equation (CQS-NLSE) describing the light propagation along the $z$ direction has the form

$$i\frac{\partial\psi}{\partial z}+\frac{1}{2}\frac{\partial^2\psi}{\partial x^2}+g_3\psi|\psi|^2+g_5\psi|\psi|^4+\psi|\psi|^6=0, \tag{21}$$

where $\psi=\psi(x,z)$ represents the normalized field amplitude, while $g_3$, $g_5$, and $g_7=1$ are coefficients related to the third-, fifth-, and seventh-order effective susceptibility, respectively. The stability of spatial solitons was investigated by varying $g_3$ and $g_5$.

Stationary solutions of the CQS-NLSE with a real propagation constant $k$ having the form $\psi(x,z)=e^{ikz}\phi(x)$ were considered. A variational approximation based on the *raised-sech Ansatz*, $\phi(x)=\Lambda[\operatorname{sech}(\sqrt{2k}x)]^{\delta}$ [216], where $\Lambda$ and $\delta$ are variational parameters, and the Vakhitov–Kolokolov (VK) stability criterion [217] were used to identify regions of stable and unstable soliton propagation. The dependence of the propagation constant on the total power, obtained from the stationary solution of Eq. (21) and using the VK criterion, is represented in Fig. 18. According to the VK criterion, the stability regions correspond to $\partial P/\partial k>0$, with $P=\int_{-\infty}^{\infty}|\phi(x)|^2\mathrm{d}x$ representing the total power.

Figure 18(a) shows that, for $g_3=+1$, $g_7=+1$, and $g_5=0$, $-1$ and $+1$, there are regions of stability corresponding to different values of the total power. In particular we note that the maximum power for the stable soliton propagation corresponds to $g_5 = -1$. Physically this occurs because the self-focusing effect due to the third- and seventh-order nonlinearity is compensated by the negative fifth-order nonlinearity. Numerical results were also reported for $-1.5 \leq g_5 \leq 1.5$ with $g_3 = +1$. For each value of $g_5$ the maximum power that allows stable soliton propagation was determined and the results, indicated in Fig. 18(b), show that large negative values of $g_5$ help to stabilize the spatial soliton. Also in [175] the beam propagation was investigated by solving numerically the CQS-NLSE using the split-step compact finite-difference method [218] using the *raised-sech Ansatz* as input for the numerical simulations. The results corroborate the conclusions based on the VK criterion. Moreover, the numerical calculations helped to identify the conditions for *supercritical collapse* induced by the seventh-order nonlinearity.

Of course the *nonlinearity management* procedure described in the previous sections may allow the verification of the theoretical results of [175] provided that a correct choice of nanoparticle volume filling fraction, laser wavelength, and light intensity is identified in order to obtain the appropriate values for $g_n$ $(n = 3, 5, 7)$.

### 7.2. Low-Intensity Excitation of Plasmonic Solitons in Metal Nanocolloids

Following a different approach than the one used for the experiments of Section 6, experimental works have been pursued by various authors aiming at the observation and manipulation of spatial solitons in plasmonic nanocolloids subject to excitation by low-power continuous-wave (CW) lasers. In [32] the authors used metallic nanoparticles (gold nanorods, silica–gold nanoshells, and gold and silver spheres) having volumes $\sim 10^2$ to $\sim 10^3$ larger than the ones used in the experiments described in Section 6. A CW laser operating at 532 nm, delivering powers up to 250 mW, was used. The response of the nanocolloids to the laser beam under the experimental conditions of [32] was manifested by the thermal response, light scattering, and gradient forces acting on the nanoparticles. The evolution of optical beams propagating through the nanocolloids was understood by analyzing a modified NLSE that includes the thermal contribution, light scattering, and the effect of a gradient force represented

Figure 18

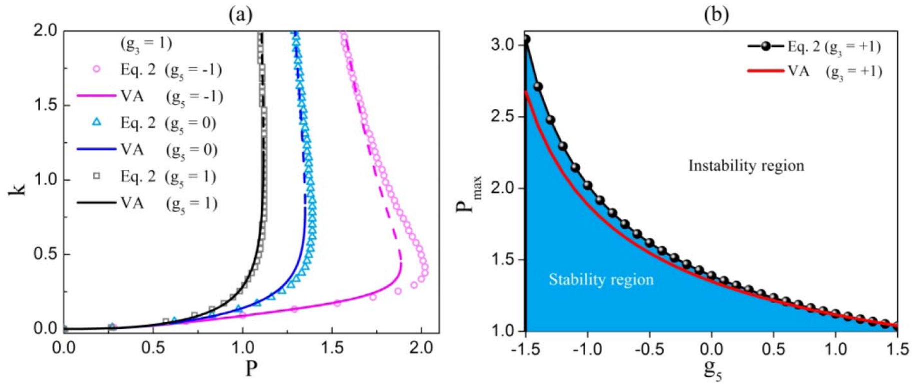

(a) The soliton propagation constant $k$ versus the total power $P$ for media with focusing third-order nonlinearity ($g_3 = 1$). Discrete points correspond to the stationary solution of Eq. (21) with $g_5 = -1$ (red circles), 0 (blue triangles) , and +1 (black squares). Dashed lines were obtained using the variational approximation. (b) The maximum power $P_{\text{max}}$ admitting the stable soliton propagation in media, as per the VK criterion, with the focusing cubic nonlinearity ($g_3 = 1$) and different values of the quintic coefficient $g_5$. Adapted with permission from [175]. Copyright 2015 by the American Physical Society.

by $\vec{F}_{\text{grad}} = \frac{1}{4}\alpha_R \nabla |\vec{E}|^2$, where $\vec{E}$ is the electric field and $\alpha_R$ represents the real part of the particle's polarizability. Assuming no particle–particle interactions, it is possible to show that the particle concentration along the beam pathway is intensity dependent and is given by $\rho = \rho_0 \exp[\alpha_R I/(4k_B T)]$, where $k_B T$ is the thermal energy and $\rho_0$ is the unperturbed uniform particle density. After manipulations following the procedure described in [219], the wave propagation can be described by

$$i\frac{\partial \psi}{\partial z} + \frac{1}{2k_0 n_h}\nabla_\perp^2 \psi + k_0(n_{\text{NP}} - n_h)\rho V_{\text{NP}}\psi + \frac{i\sigma\rho}{2}\psi - k_0|\Delta n_T|\psi = 0, \tag{22}$$

where $k_0 = 2\pi/\lambda_0$ is the vacuum wavenumber, and $\sigma$ is the Rayleigh scattering cross section [220]. The third, fourth, and fifth terms in Eq. (22) represent a Kerr-type nonlinearity, scattering losses, and thermal defocusing response, respectively. The volume fraction along the beam pathway is given by $f(I) = f(0)\exp[\alpha I/(4k_B T)]$, and $\Delta n_T = (\partial n_h/\partial T)(T - T_0)(1 - f)$ represents the variation of the colloid refractive index due to the temperature change that occurs because of the light absorption by the nanoparticles. $T$ is the spatial temperature distribution in the presence of the laser beam and $T_0$ is the initial temperature of the colloid. In [32] the values of $\Delta n_T$ in the experiments with the nanorods and nanoshells were negligible because of the large detuning between the laser frequency and $\omega_{\text{LSP}}$. However, the thermal contribution was important in the experiments with nanospheres because of the large optical absorption at the laser wavelength used. The intensity dependence of $\rho$ is due to the attraction (repulsion) of the nanoparticles toward (away from) the beam according to the sign of $\alpha_R$. As can be seen in Fig. 5, the value of $\alpha_R$ at 532 nm is negative for the nanorods and nanoshells and the particles are expelled from the highest intensity region. In the nanospheres the opposite occurs, as demonstrated in [32]. Figure 19 illustrates the effects of attraction and repulsion of the nanoparticles with respect to the laser beam that contributes to the expression given above for $f(I)$.

In both cases the spatial rearrangement of the particles produces a self-focusing nonlinearity that induces trapping of the optical beam.

Figures 20 and 21 illustrate the beam trapping in the colloids with nanorods and nanoshells, respectively.

Recently the experiments of [32] were further extended and the results in [221] demonstrated the possibility of guiding a strong infrared beam (at 1064 nm) through a weak soliton-forming beam (at 532 nm) with basis on the effects included in Eq. (22). Experiments of cross-phase modulation with both beams contributing simultaneously to the self-focusing nonlinearity were also reported.

More recently the possibility of self-structuring of a laser beam propagating in a metal nanocolloid was proposed [222] by considering the gradient forces as in Eq. (22).

Figure 19

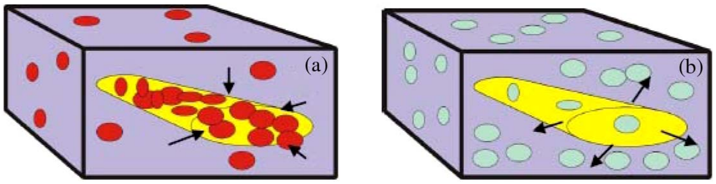

High-intensity beam (a) attracting nanoparticles with positive polarizabilities and (b) repelling nanoparticles with negative polarizabilities. Adapted with permission from [219].

However, optical gain was considered assuming the addition of dye molecules dissolved in the nanocolloid. By analyzing the competition between diffraction and nonlinearity together with compensation between gain and loss, the authors demonstrated theoretically the possibility of dissipative breathing vortex solitons formation, which they propose to be used for selective dynamic photonic tweezing of nanoparticles.

One conclusion deduced from [32,221,222] is that the overall response of the nanocolloids is analogous to the response described in Section 6 for cubic–quintic saturable nonlinear media, and therefore the *nonlinearity management* procedure can be applied in those cases aiming further developments. Notice also that in this case by selecting the optical frequency around $\omega_{\mathrm{LSP}}$ the nature of the light–matter interaction changes, allowing engineering the focusing–defocusing response of the effective susceptibilities.

Although the works described in [32,221,222] are very interesting because the experiments requires low-intensity light, one disadvantage with respect to the approach described in Section 6, based on the electronic response of the nanoparticles, is the slow time response that limits all-optical switching applications. On the other hand, according to the authors of [221], the guiding of an intense beam by a weak beam

Figure 20

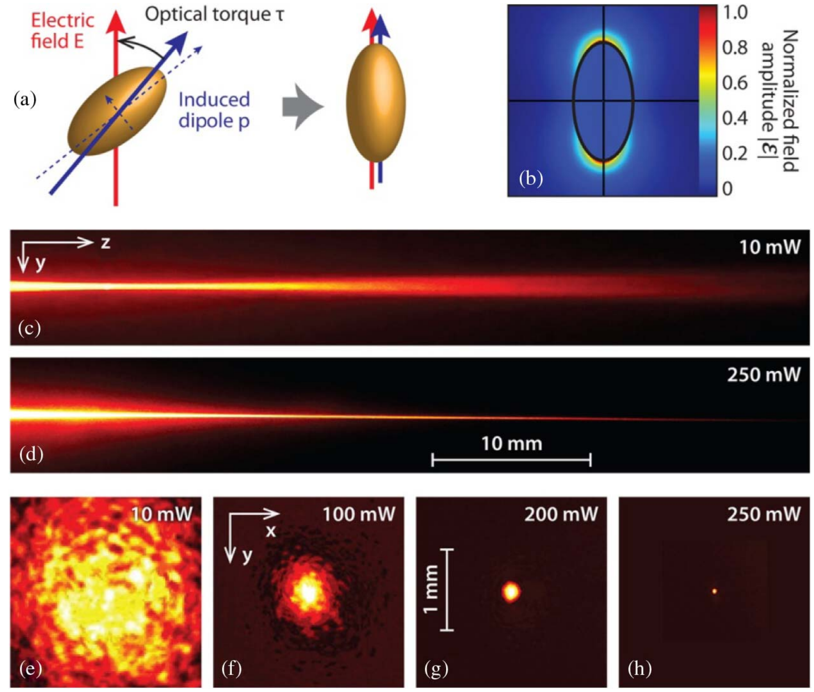

(a) Orientation of gold nanorods along the electric field $\vec{E}$ of a linearly polarized beam. (b) Field distribution around the nanorod at the longitudinal plasmon resonance. (c) Linear diffraction of a low-power beam (10 mW) when injected into an aqueous suspension of gold nanorods. (d) Formation of a stable self-trapped filament at 250 mW over 5 cm (25 diffraction lengths) mediated by the negative polarizability of the colloid. (e)–(h) Beam profiles observed after 5 cm of propagation at different input power levels, showing the transition from diffractive broadening at 10 mW to self-trapping at 250 mW. For reasons of visibility, the output beam profiles have been normalized with respect to their individual peak intensities. Reprinted with permission from Fardad *et al.*, Nano Lett., **14**, 2498–2504 (2014) [32]. Copyright 2014 American Chemical Society.

demonstrated in the experiment opens new doors for applications in optofluidics and biophotonics.

### 7.3. Nonlinearity Management in Plasmonic Metamaterials

The plasmonic nanocolloids considered in the previous sections represent a class of optical metamaterials (OMMs) in the sense that they are artificially structured materials engineered to exhibit exotic optical properties when interacting with the electromagnetic field. However, one fascinating result obtained from the study of OMMs is the possibility of materials with negative refractive index that simultaneously present negative electric permittivity, $\varepsilon$, and negative magnetic permeability, $\mu$ (see [223] and references therein). The existence of this kind of OMM corroborates the predictions that the refractive index, $n = -\sqrt{\varepsilon\mu}$, when both $\varepsilon, \mu < 0$, is an acceptable physical solution of Maxwell's equations [224]. A negative value for the linear refractive index leads to new phenomena such as described by the reversal Snell's law [224] and reversal Doppler effect [225].

In the context of NL optics the OMMs represent a new alternative to obtain desired NL responses with an adequate control and improvement in relation to traditional materials (see, for example, [226]). A special class of NL metamaterials is the plasmonic metamaterials, which are typically composed of various combinations of metal nanostructures hosted in dielectric materials that exploit surface plasmons to achieve optical properties not seen in nature [227]. For instance, plasmonic metamaterials

Figure 21

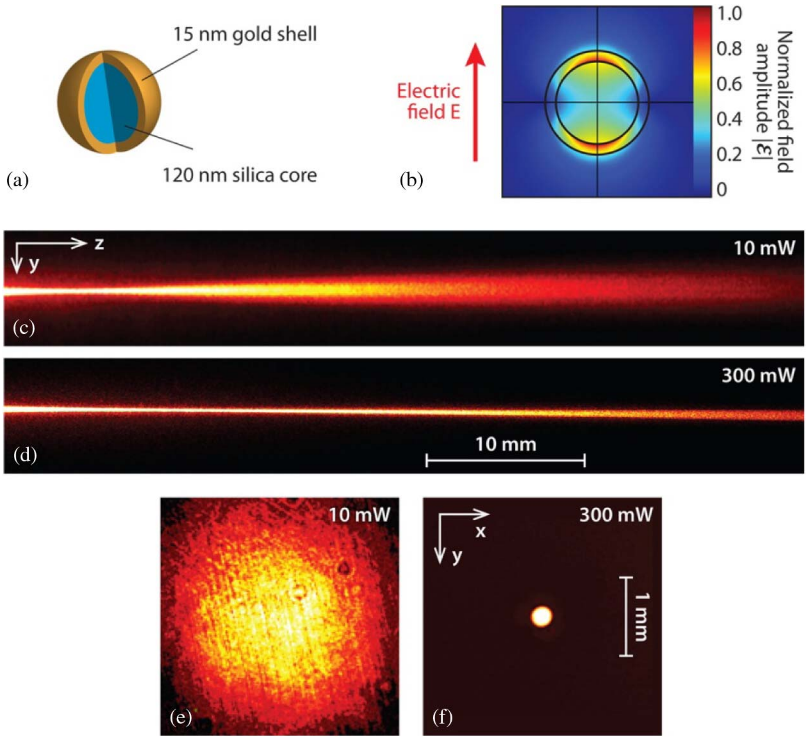

(a) Schematic of a silica–gold core–shell particle and (b) field distribution at its plasmon resonance. (c) Linear diffraction pattern at 10 mW and (d) stable soliton formation in the NP suspension at 300 mW. (e),(f) Corresponding normalized output beam profiles after a propagation distance of 5 cm. Reprinted with permission from Fardad *et al.*, Nano Lett., **14**, 2498–2504 (2014) [32]. Copyright 2014 American Chemical Society.

constituted of arrays of L-shaped gold NPs [Fig. 22(a)] allow efficient control on the second-order NL response when the nanostructures are positioned in different ways, as illustrated in Figs. 22(b)–22(d) [228].

Figures 22(e) and 22(d) illustrate the experimental and theoretical normalized second-harmonic generation (SHG) intensities as a function of the linear input polarization angle, for the samples exemplified in Figs. 22(c) and 22(d), respectively. The dependence of the SHG intensity with the direction of the input electric field polarization is similar, although the SHG efficiencies are different. This is due to the long-range coupling between the particles that depends on their arrangements and shapes [228]. A similar procedure to control the second-order NL response of different systems was performed by depositing nanoscopic inclusions of plasmonic metamaterials and controlling their size, shape, and symmetry [229]. Changes in the spectral profile of the SHG were reported for metamaterials with different nanoinclusion designs when the contributions of each component of the second-order susceptibility tensor were analyzed, as shown in Fig. 23. Therefore, a possibility for *nonlinearity management* of plasmonic metamaterials may be achieved by varying the structure of the plasmonic inclusions and metamolecular ordering, which can lead to large improvements in its NL response.

On the other hand, following the *nonlinearity management* procedure described in Section 5 it is also possible to control the optical response of the OMM with complex inclusions designs. The theoretical and numerical works presented in [111,230] show that the NL response of metamaterials can be manipulated by the selection of plasmonic NPs with controlled sizes and shapes to achieve nonlinearity enhancement by several orders of magnitude. For instance, large NL phase shift, $\Delta\Phi_{NL}$, at very short propagation distances can be obtained by impregnating metallic NPs (monomers or

Figure 22

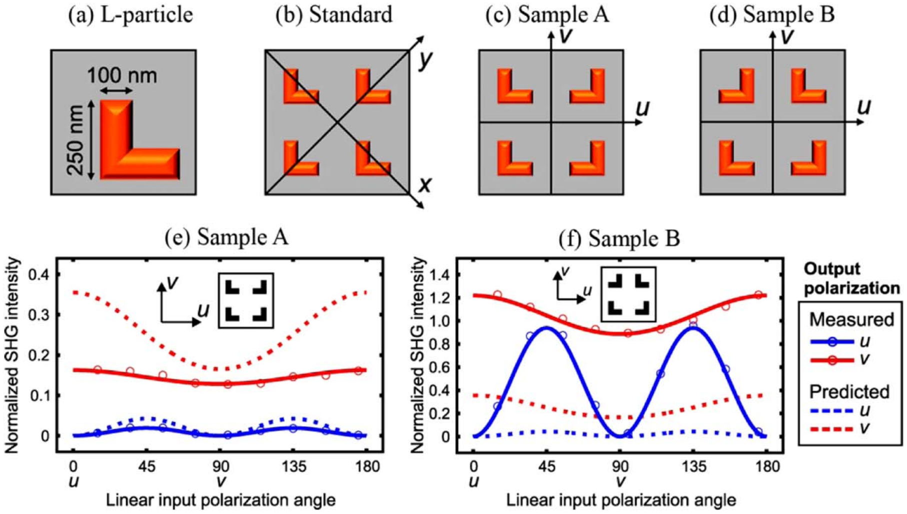

(a) Dimensions of the L-shaped gold particles. (b)–(d) Layouts of the investigated samples and the coordinate systems. The normalized SHG intensity as a function of the linear input polarization angle measured from *u* direction is illustrated by (e) Sample A and (f) Sample B. The circles are experimental data and the solid lines are fits to the measured points. Dashed lines are the predicted responses calculated by the orientational average of the responses of individual particles. Adapted with permission from Husu *et al.*, Nano Lett., **12**, 673–677 (2012) [228]. Copyright 2012 American Chemical Society.

dimers) into waveguides, as shown in Fig. 24. For an average power of 1.6 mW, it is possible to observe that after a propagation distance of 1 μm, the $\Delta\Phi_{NL}$ obtained in chalcogenide waveguides can be enhanced by 2 orders of magnitude when elliptical gold NPs are introduced, whereas an enhancement of 4 orders of magnitude can be obtained with dimers of elliptical gold NPs. However, for propagation distances greater than ~5 μm, $\Delta\Phi_{NL}$ saturates due to the high-intensity losses caused by the metal NPs. Nevertheless, the use of the *nonlinearity management* procedure, discussed in Section 5, may reduce the dissipative effects allowing adequate control and optimization of $\Delta\Phi_{NL}$ for different propagation distances, and then $\Delta\Phi_{NL}$ may assume appropriate values for applications in all-optical circuits. In this way, the experiments of Subsection 6.4 can be extended for plasmonic metamaterials with more complex inclusions designs, having as additional variable to control the NL response the different shapes and sizes of the plasmonic nanostructures.

The NL response of plasmonic metamaterials based on chains of metal NPs with alternating sizes, relatively small interparticle spacing within each chain, and relatively large spacing between chains, were analyzed numerically in [111]. The binary size arrangements considered exhibit electric field enhancement factor, $E_x/E_0$, for both NPs that depends on the ratio between their sizes and the incident light frequency, as shown in Figs. 25(a)–25(c). For structures with homogeneous NP distribution [Fig. 25(a)] the optical field is enhanced, at the center of the NPs, by a maximum factor of 33 at ~432 nm, which corresponds to the dipolar plasmon resonance in spherical NPs with a diameter of ≈2.5 nm and spacing between particles of 3 nm. However, small differences in size between neighboring NPs produce large increase in the electric field enhancement factor [see Figs. 25(b)–25(c)], due to cascaded plasmon resonance induced on the smaller NP due to the action of the enhanced near field

Figure 23

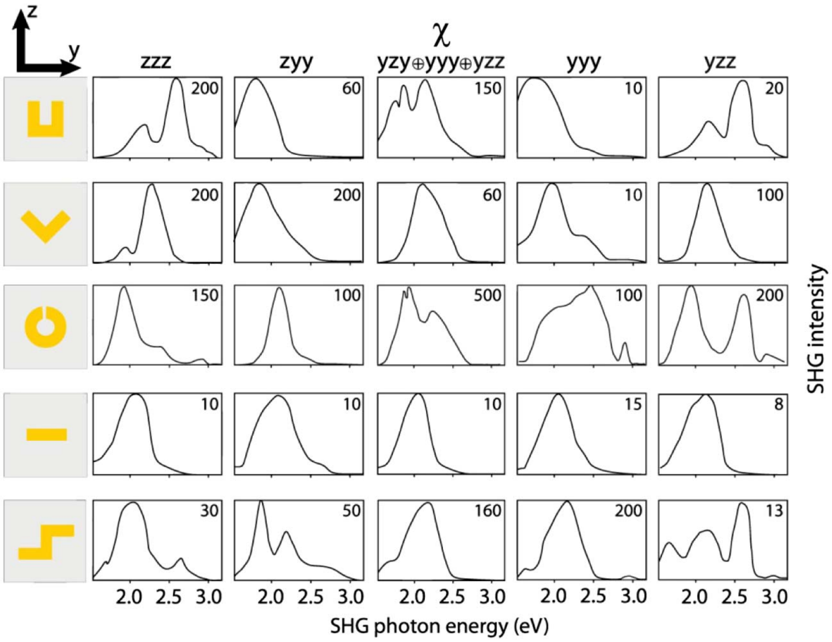

(a) SHG spectra for metamaterials featuring a variety of designs. The values given as insets represent the peak value of each spectrum on an arbitrary scale. The spectra in the center column represent a convolution of contributions from three independent SHG tensor components. Reprinted with permission from [229]. Copyright 2011 Springer.

around the larger NP. For instance, neighboring NPs with a volume ratio of 30 [Fig. 25(c)] show a maximum $E_x/E_0$ of ~97, which is approximately 3 times the factor calculated for structures with identical neighbor particles. As is well known, a large electric field enhancement factor leads to enhanced NL response of plasmonic metamaterials [95]. In fact, Fig. 25(d) shows an enhanced figure of merit of the cubic nonlinearity defined as $g^{(3)}/\alpha$, where $g^{(3)}$ is a complex third-order susceptibility enhancement factor due to effects of cascaded plasmon resonance and $\alpha$ is the linear absorption coefficient. Significant figure-of-merit enhancement, related to third-order refractive index and absorption coefficient, is observed in plasmonic metamaterials constituted by periodic binary structure, with a volume ratio of 30 (blue points), compared to identical neighboring particles (red points). The numerical results predicted for cubic nonlinearity can be extended for high-order nonlinearities, since the electric field enhancement increases significantly the contributions of effective high-order susceptibilities because they depend on higher powers of the applied electric field, as shown in Section 4.

Nowadays great efforts are devoted to the study of new optical phenomena induced by different kinds of metamaterials. One of the most explored topics is the light propagation in metamaterials with negative refractive index, since significant changes are predicted in comparison to traditional materials. In addition, because NL metamaterials may present very large optical response, it is reasonable to predict that light propagation may be affected by high-order NL contributions. Based on this reasoning several theoretical proposals and numerical simulations were performed to analyze the evolution of the light fields being affected by complex high-order susceptibilities (quintic and cubic–quintic nonlinearities) [231] and high-order dispersion [148], which give rise to effects such as modulation instability [148,231], optical solitons [232,233], and rogue waves [234].

Figure 24

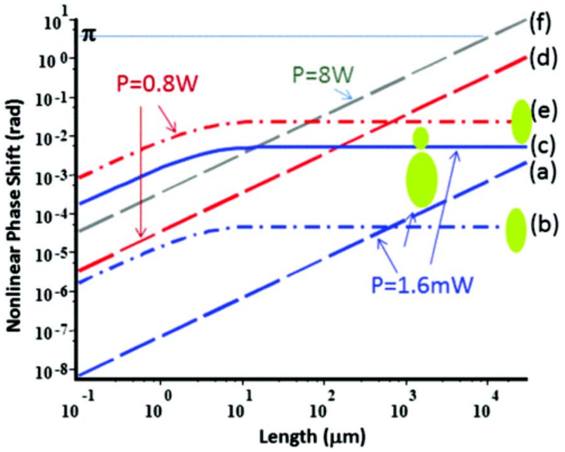

Nonlinear phase shift in the 1 μm$^2$ chalcogenide waveguide: (a) input power of 1.6 mW, no plasmonic enhancement; (b) input power of 1.6 mW, nonlinearity enhanced by the elliptical Au nanoparticles with the filling fraction of 0.001; (c) input power of 1.6 mW, nonlinearity enhanced by the dimers of elliptical Au nanoparticles with the filling fraction of 0.001; (d) input power of 0.8 W, no plasmonic enhancement; (e) input power of 0.8 W, nonlinearity enhanced by the elliptical Au nanoparticles with the filling fraction of 0.001; (f) input power of 8 W, no plasmonic enhancement. Figure 7 reprinted with permission from Khurgin and Sun, Phys. Rev. A, **88**, 053838 (2013) [230]. Copyright 2013 by the American Physical Society.

The modulation instability effect in NL metamaterials exhibiting dispersive magnetic permeability, $\mu(\omega)$, and electric permittivity, $\varepsilon(\omega)$, can be controlled through the materials structure design. Additionally, due to the large NL response of metamaterials at moderate intensities, HON can play a relevant role in the evolution of the light fields. For instance, the impact of the quintic nonlinearity on the cross-modulation instability (XMI) scheme with negative-index metamaterials was analyzed theoretically by considering two interacting light beams described by two coupled modified NLSEs based on the dispersive Drude model [231]. Figures 26(a) and 26(b) show the XMI gain spectra versus the frequency difference of waves copropagating in a negative-index metamaterial with equal perturbation frequencies in the normal and anomalous dispersion regimes, respectively. The results are shown in Fig. 26. The green and blue lines corresponding to a cubic–quintic medium show a gain of modulation larger than for a cubic medium (red line) in both regimes. The effect is more important in the anomalous dispersion regime, but it covers a wider frequency region in the normal dispersion regime. Similar results were obtained when the instability analysis was performed with different perturbation frequencies in both dispersion regimes, as shown in Figs. 26(c) and 26(d).

Figure 25

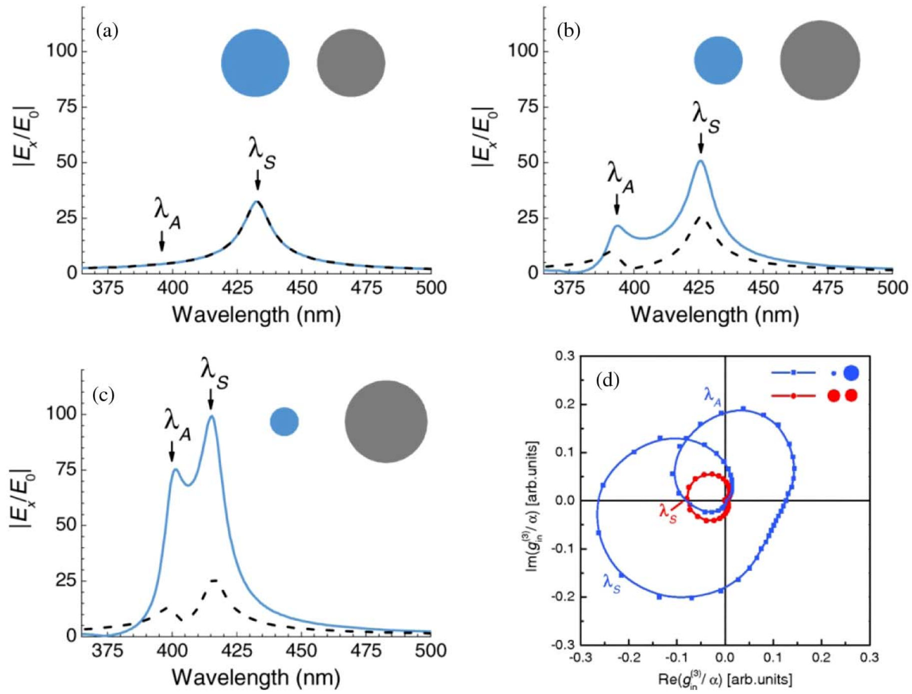

Magnitude of the electric field enhancement factor inside adjacent small (solid line) and large (dashed line) nanoparticles, for (a) identical sizes, (b) a volume ratio of 4.8, and (c) a volume ratio of 30. (d) Complex enhanced figure-of-merit of the third-order NL optical response of a plasmonic metamaterial containing silver nanoparticles with a single size (radius = 1 nm) and of a cascaded plasmonic metamaterial with a nearest-neighbor volume ratio of 30. The legend shows the corresponding unit cell of the periodic metamaterial. The labels $\lambda_A$ and $\lambda_S$ correspond to the antisymmetric and symmetric modes, respectively. Figures 3(a)–3(c) and Fig. 6 reprinted with permission from Toroghi and Kik, Phys. Rev. B, **85**, 045432 (2012) [111]. Copyright 2012 by the American Physical Society.

Numerical simulations were also reported considering higher-order dispersive and dissipative effects [148]. Figure 27(a) shows that the modulation gain for a nondissipative system with dispersion effect up to the fourth order increases with the ratio between

Figure 26

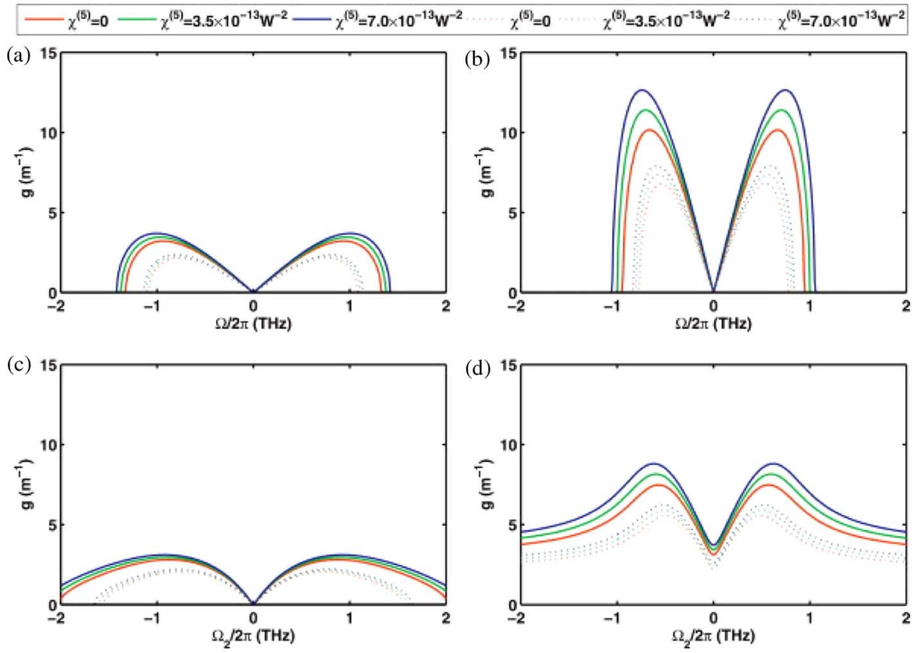

Impact of the quintic nonlinearity on the XMI gain spectra with pump and probe incident power of 100 W, in the (a),(c) normal and (b),(d) anomalous dispersion regimes with (a),(b) equal and (c),(d) different perturbation frequencies. The dashed lines are the gain spectra for the corresponding solid lines after propagation by 2 km considering attenuation. Reprinted from Liu *et al.*, "Modulation instability induced by cross-phase modulation in negative materials with higher-order nonlinearity," Opt. Commun. **339**, 66–73 [231]. Copyright 2015, with permission from Elsevier.

Figure 27

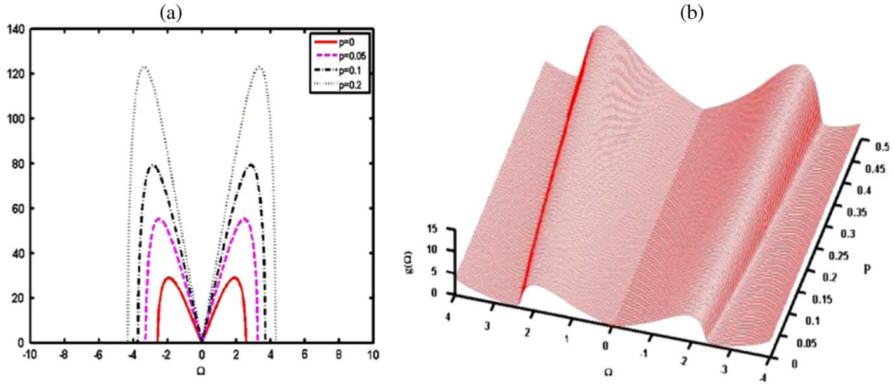

Modulation instability gain as a function of perturbation frequency Ω and higher-order nonlinear parameter *p* for (a) nondissipative and (b) dissipative systems. Reprinted from Saha and Sarma, "Modulation instability in nonlinear metamaterials induced by cubic-quintic nonlinearities and higher-order dispersion effects," Opt. Commun. **291**, 321–325 [148]. Copyright 2013, with permission from Elsevier.

the fifth- and third-order NL parameters, $p$, in accordance with the results obtained in [231]. Then, when the dissipation effects are considered, the strength of the modulation gain decreases due to the intensity losses and distortions at the ends of the sidebands are observed, as shown in Fig. 27(b). These distortions were also observed in the experiments of Subsection 6.4. Nevertheless, the modulation gain is still higher for materials with quintic nonlinearities, as in the case discussed in Subsection 6.4.

Moreover, since the permeability and permissivity of metamaterials present dispersive behavior, narrow bandwidth beams having different central frequencies can experience regions of positive and negative diffraction that depend on the sign of the refractive index, $n(\omega)$. This characteristic allows the introduction of a new procedure to arrest the collapse of a probe beam, propagating in a region with positive refractive index, by using a XPM scheme, where a pump beam feels a negative refractive index. In [235] the theoretical and numerical evolution of the probe and pump beams propagating through a NL metamaterial was investigated. When the refractive index is positive, strong self-focusing may overcome the positive diffraction, and the beam is quickly compressed with an exponential increase of the peak intensity leading to the beam collapse (catastrophic self-focusing). However, when the pump beam feels a negative refractive index, the effect of negative diffraction competing with the focusing nonlinearity may lead to spatial broadening of the beam and consequently to a progressive decrease of the peak intensity along the propagation. Because the NL response is strong, a probe beam which propagates feeling a positive refractive index, initially may suffer a spatial compression with increase of its peak intensity. However, due to the decrease of the pump beam peak intensity, the NL contribution induced by XPM on the probe beam will decrease and as a result the probe beam intensity will decrease until returning to the linear regime, avoiding the beam collapse [235]. These effects as well as other analogous phenomena will enable *nonlinearity management* in metamaterials opening new routes for various applications. Notice that plasmonic metamaterials are suitable candidates to corroborate these theoretical forecasts due to their large nonlinearity and the possibility of managing their NL response.

In the context of soliton physics, a large number of theoretical publications reinforced with numerical simulations are found in negative-index metamaterials supported by cubic nonlinearity (see, for example, [226,236]). However, since modulation instability, which is a precursor of solitons, is affected by HON, the formation and propagation of solitons is also influenced by HON. Actually, theoretical predictions show that quintic nonlinearity in negative-index metamaterials can prevent beam collapse, in analogy to traditional materials. In addition, the quintic nonlinearity is essential for formation of bright–dark soliton coupled states [237]. When the quintic nonlinearity is weak, i.e., it is not sufficiently large to produce the level of saturation needed to prevent the beam collapse, the NL diffraction allows stabilization of solitons in negative-index metamaterials [238]. Of course, due to the high complexity in the manufacture of metamaterials, most of the theoretical studies formulated for negative-index metamaterials lack experimental corroboration up to the present. Naturally plasmonic metamaterials are an interesting option for the observation of these new phenomena, and the progress in the materials fabrication may lead to applications in the future. Therefore, the possibility of *nonlinearity management* as discussed at the beginning of this section, with focus on the influence of the quintic nonlinearity to control the cross-phase modulation, is highly attractive.

## 8. CONCLUSIONS AND OUTLOOK

The field of nonlinear optics, being more than 50 years old, still offers new possibilities to manage light. As described along the previous pages, by adjusting the metal NP volume filling fraction of the samples and working with appropriate light intensities, various nanocolloid compositions with tailored high-order nonlinearities were investigated. Hence, the experiments reviewed in this paper demonstrate that metal nanocolloids are versatile platforms for nonlinear optical studies and the results reported may stimulate the synthesis of novel metal–dielectric nanocomposites (based on inorganic glasses or polymers) with optimized characteristics for specific photonic devices.

Finally we want to comment that there is a large volume of theoretical and computational studies with proposals related to the propagation of light in nonlinear media, with analogies in fields like Bose–Einstein condensation and condensed matter physics. The *nonlinearity management* may be highly useful for further work along some lines already discussed in the literature. For instance, the coherent interaction between solitons, their stability under spin-orbit coupling, the generation of patterns by parametric instability, spatial-temporal solitons (light bullets), and the exploitation of the possible analogies with solitons in magnetic materials and superconductors are examples of potential extensions of the works reported in this paper. The *nonlinearity management* procedure presented here for metal nanocolloids is a suitable way to design new experiments related to high-order optical effects and spectroscopic applications. Therefore, this is a challenging area since many basic phenomena studied from the theoretical point of view were not investigated by experiments up to now.

## FUNDING

Conselho Nacional de Desenvolvimento Científico e Tecnológico (CNPq); Fundação de Amparo à Ciência e Tecnologia do Estado de Pernambuco (FACEPE); National Institute of Photonics (INCT de Fotônica-INFO); PRONEX/CNPQ/FACEPE.

## ACKNOWLEDGMENT

We acknowledge our collaborators in the original works reviewed in this paper: Edilson L. Falcão-Filho, Luís Arturo Gomez, Anderson S. L. Gomes, Boris A. Malomed, Emeric Bergmann, Pierre-François Brevet, Anderson M. Amaral, Georges Boudebs, André Galembeck, Lucio H. Acioli, Marcio Miranda, Leonardo de S. Menezes, and Kelly C. Jorge.

## REFERENCES

1. M. R. Gonçalves, “Plasmonic nanoparticles: fabrication, simulation and experiments,” J. Phys. D **47**, 213001 (2014).
2. M. Gajc, H. B. Surma, A. Klos, K. Sadecka, K. Orlinski, A. E. Nikolaenko, K. Zdunek, and D. A. Pawlak, “Nanoparticle direct doping: novel method for manufacturing three-dimensional bulk plasmonic nanocomposites,” Adv. Funct. Mater. **23**, 3443–3451 (2013).
3. P. W. de Oliveira, C. Becker-Willinger, and M. H. Jilavi, “Sol-gel derived nanocomposites for optical applications,” Adv. Eng. Mater. **12**, 349–361 (2010).
4. B. Karmakar, K. Radermann, and A. L. Stepanov, *Glass Nanocomposites (Synthesis, Properties and Applications)*, Micro & Nano Technologies Series (Elsevier, 2016).
5. Y. Gogotsi, *Nanomaterials Handbook* (CRC Press, 2006).
6. N. Faraji, W. M. M. Younus, A. Kharazmi, E. Saion, M. Shahmiri, and N. Tamchek, “Synthesis, characterization and nonlinear optical properties of silver/PVA nanocomposites,” J. Eur. Opt. Soc. **7**, 12040 (2012).
7. Y. Xia, Y. Xiong, B. Lim, and S. E. Skrabalak, “Shape-controlled synthesis of metal nanocrystals: simple chemistry meets complex physics?” Angew. Chem. **48**, 60–103 (2008).

8. N. Bloembergen, *Nonlinear Optics* (W. A. Benjamin, 1965).
9. S. A. Maier, *Plasmonics–Fundamentals and Applications* (Springer, 2007).
10. M. Faraday, "The Bakerian lecture: experimental relations of gold (and other metals) to light," Philos. Trans. R. Soc. London **147**, 145–181 (1857).
11. C. F. Bohren and D. H. Huffman, *Absorption and Scattering of Light by Small Particles* (Wiley-VCH Verlag, 1998).
12. M. M. Alvarez, J. T. Khoury, G. Schaaff, M. N. Shafigullin, I. Vezmar, and R. L. Whetten, "Optical absorption spectra of nanocrystal gold molecules," J. Phys. Chem. B **101**, 3706–3712 (1997).
13. A. D. Rakić, A. B. Djurišić, J. M. Elazar, and M. L. Majewski, "Optical properties of metallic films for vertical-cavity optoelectronic devices," Appl. Opt. **37**, 5271–5283 (1998).
14. A. Alabastri, S. Tuccio, A. Giugni, A. Toma, C. Liberale, G. Das, F. De Angelis, E. Di Fabrizio, and R. P. Zaccaria, "Molding of plasmonic resonances in metallic nanostructures: dependence of the non-linear electric permittivity on system size and temperature," Materials **6**, 4879–4910 (2013).
15. P. K. Jain and M. A. El-Sayed, "Surface plasmon resonance sensitivity of metal nanostructures: physical basis and universal scaling in metal nanoshells," J. Phys. Chem. C **111**, 17451–17454 (2007).
16. S. Link and M. A. El-Sayed, "Optical properties and ultrafast dynamics of metallic nanocrystals," Ann. Rev. Phys. Chem. **54**, 331–366 (2003).
17. U. Kreibig, B. Schmitz, and H. D. Breuer, "Separation of plasmon-polariton modes of small metal particles," Phys. Rev. B **36**, 5027–5030 (1987).
18. A. Kawataba and R. Kubo, "Electronic properties of fine metallic particles. II. Plasma resonance absorption," J. Phys. Soc. Jpn. **21**, 1765–1772 (1966).
19. W. P. Halperin, "Quantum size effects in metal particles," Rev. Mod. Phys. **58**, 533–606 (1986).
20. W. A. de Heer, "The physics of simple metal clusters: experimental aspects and simple models," Rev. Mod. Phys. **65**, 611–676 (1993).
21. J. Lermé, H. Baida, C. Bonnet, M. Broyer, E. Cottancin, A. Crut, P. Maioli, N. Del Fatti, F. Vallée, and M. Pellarin, "Size dependence of the surface plasmon resonance damping in metal nanospheres," J. Phys. Chem. Lett. **1**, 2922–2928 (2010).
22. J. Lermé, "Size evolution of the surface plasmon resonance damping in silver nanoparticles: confinement and dielectric effects," J. Phys. Chem. C **115**, 14098–14110 (2011).
23. J. Lermé, C. Bonnet, M.-A. Lebeault, M. Pellarin, and E. Cottancin, "Surface plasmon resonance damping in spheroidal metal particles: quantum confinement, shape, and polarization dependences," J. Phys. Chem. C **121**, 5693–5708 (2017).
24. M. A. Garcia, "Surface plasmons in metallic nanoparticles: fundamentals and applications," J. Phys. D **44**, 283001 (2011).
25. A. Pinchuk, G. von Plessen, and U. Kreibig, "Influence of interband electronic transitions on the optical absorption in metallic nanoparticles," J. Phys. D **37**, 3133–3139 (2004).
26. P. N. Prasad, *Nanophotonics* (Wiley, 2004).
27. L. Novotny and B. Hecht, *Principles of Nano-Optics* (Cambridge University, 2006).
28. E. Hao and G. C. Schatz, "Electromagnetic fields around silver nanoparticles and dimers," J. Chem. Phys. **120**, 357–366 (2004).
29. S. A. Kalele, N. R. Tiwari, S. W. Gosavi, and S. K. Kulkarni, "Plasmon-assisted photonics at the nanoscale," J. Nanophotonics **1**, 012501 (2007).

30. S. Link and M. A. El-Sayed, “Spectral properties and relaxation dynamics of surface plasmon electronic oscillations in gold and silver nanodots and nanorods,” J. Phys. Chem. B **103**, 8410–8426 (1999).
31. V. Sharma, K. Park, and M. Srinivasarao, “Colloidal dispersion of gold nanorods: historical background, optical properties, seed-mediated synthesis, shape separation and self-assembly,” Mater. Sci. Eng. R **65**, 1–38 (2009).
32. S. Fardad, A. Salandrino, M. Heinrich, P. Zhang, Z. Chen, and D. N. Christodoulides, “Plasmonic resonant solitons in metallic nanosuspensions,” Nano Lett. **14**, 2498–2504 (2014).
33. J. Saade and C. B. de Araújo, “Synthesis of silver nanoprisms: a photochemical approach using light emission diodes,” Mater. Chem. Phys. **148**, 1184–1193 (2014).
34. U. Kreibig and M. Völlmer, *Optical Properties of Metal Clusters*, Springer Series in Material Science (Springer, 1995).
35. B. T. Draine and P. J. Flatau, “Discrete-dipole approximation for scattering calculations,” J. Opt. Soc. Am. A **11**, 1491–1499 (1994).
36. R. X. Bian, R. C. Dunn, X. S. Xie, and P. T. Leung, “Single molecule emission characteristics in near-field microscopy,” Phys. Rev. Lett. **75**, 4772–4775 (1995).
37. J. Zhao, A. O. Pinchuk, J. M. McMahon, S. Li, L. K. Ausman, A. L. Atkinson, and G. C. Schatz, “Methods for describing the electromagnetic properties of silver and gold nanoparticles,” Acc. Chem. Res. **41**, 1710–1720 (2008).
38. J. Parsons, C. P. Burrows, J. R. Sambles, and W. L. Barnes, “A comparison of techniques used to simulate the scattering of electromagnetic radiation by metallic nanostructures,” J. Mod. Opt. **57**, 356–365 (2010).
39. M. A. Yurkin, A. G. Hoekstra, R. S. Brock, and J. Q. Lu, “Systematic comparison of the discrete dipole approximation and the finite difference time domain method for large dielectric scatterers,” Opt. Express **15**, 17902–17911 (2007).
40. B. T. Draine, “The discrete dipole approximation for light scattering by irregular targets,” in *Light Scattering by Nonspherical Particles: Theory, Measurements, and Applications*, M. I. Mishchenko, J. W. Hovenier, and L. D. Travis, eds. (Academic, 2000), Chap. 5, pp. 131–145.
41. B. Draine and P. Flatau, “User guide for the discrete dipole approximation code DDSCAT.6.0,” arXiv:astro-ph/0309069 (2003).
42. V. G. Farafonov, V. B. Il’in, and M. S. Prokopjeva, “Light scattering by multilayered nonspherical particles: a set of methods,” J. Quantum Spectrosc. Radiat. Transfer **79–80**, 599–626 (2003).
43. T. Wriedt and U. Comberg, “Comparison of computational scattering methods,” J. Quantum Spectrosc. Radiat. Transfer **60**, 411–423 (1998).
44. J. W. Hovenier, K. Lumme, M. I. Mishchenko, N. V. Voshchinnikov, D. W. Mackowski, and J. Rahola, “Computations of scattering matrices of four types of non-spherical particles using diverse methods,” J. Quantum Spectrosc. Radiat. Transfer **55**, 695–705 (1996).
45. T. Wriedt, J. Hellmers, E. Eremina, and R. Schuh, “Light scattering by single erythrocyte: comparison of different methods,” J. Quantum Spectrosc. Radiat. Transfer **100**, 444–456 (2006).
46. A. Zangwill and P. Soven, “Density-functional approach to local-field effects in finite systems: photoabsorption in the rare gases,” Phys. Rev. A **21**, 1561–1572 (1980).
47. N. J. Halas, S. Lal, W.-S. Chang, S. Link, and P. Nordlander, “Plasmons in strongly coupled metallic nanostructures,” Chem. Rev. **111**, 3913–3961 (2011).
48. E. Prodan, P. Nordlander, and N. J. Halas, “Effects of dielectric screening on the optical properties of metallic nanoshells,” Chem. Phys. Lett. **368**, 94–101 (2003).

49. J. Zuloaga, E. Prodan, and P. Nordlander, “Quantum plasmonics: optical properties and tunability of metallic nanorods,” ACS Nano **4**, 5269–5276 (2010).
50. S. Lal, S. Link, and N. J. Halas, “Nano-optics from sensing to waveguiding,” Nat. Photonics **1**, 641–648 (2007).
51. D. Ricard, P. Roussignol, and C. Flytzanis, “Surface-mediated enhancement of optical phase conjugation in metal colloids,” Opt. Lett. **10**, 511–513 (1985).
52. F. Hache, D. Ricard, and C. Flytzanis, “Optical nonlinearities of small metal particles: surface-mediated resonance and quantum size effects,” J. Opt. Soc. Am. B **3**, 1647–1655 (1986).
53. C. L. Haynes, A. J. Haes, A. D. McFarland, and R. P. V. Duyne, “Nanoparticles with tunable localized surface plasmon resonance,” in *Topics in Fluorescence Spectroscopy*, J. R. Lakowicz and C. D. Geddes, eds. (Springer, 2005), pp. 47–99.
54. L. A. Gomez, C. B. de Araújo, A. M. Brito-Silva, and A. Galembeck, “Influence of stabilizing agents on the nonlinear susceptibility of silver nanoparticles,” J. Opt. Soc. Am. B **24**, 2136–2140 (2007).
55. L. A. Gomez, C. B. de Araújo, A. M. Brito-Silva, and A. Galembeck, “Solvent effects on the linear and nonlinear optical response of silver nanoparticles,” Appl. Phys. B **92**, 61–66 (2008).
56. E. Almeida, A. C. L. Moreira, A. M. Brito-Silva, A. Galembeck, C. P. Melo, L. de S. Menezes, and C. B. de Araújo, “Ultrafast dephasing of localized surface plasmons in colloidal silver nanoparticles: the influence of stabilizing agents,” Appl. Phys. B **108**, 9–16 (2012).
57. A. Crut, P. Maioli, F. Vallée, and N. Del Fatti, “Linear and ultrafast nonlinear plasmonics of single nano-objects,” J. Phys. Condens. Matter **29**, 123002 (2017).
58. U. Kreibig and L. Genzel, “Optical absorption of small metallic particles,” Surf. Sci. **156**, 678–700 (1985).
59. H. Hövel, S. Fritz, A. Hilger, U. Kreibig, and M. Vollmer, “Width of cluster plasmon resonances: bulk dielectric functions and chemical interface damping,” Phys. Rev. B **48**, 18178–18188 (1993).
60. A. Pinchuck, U. Kreibig, and A. Hilger, “Optical properties of metallic nanoparticles: influence of interface effects and interband transitions,” Surf. Sci. **557**, 269–280 (2004).
61. D. Gall, “Electron mean free path in elemental metals,” J. Appl. Phys. **119**, 085101 (2016).
62. P. C. Lee and D. Meisel, “Adsorbed and surface enhanced Raman of dyes on silver and gold sols,” J. Phys. Chem. **86**, 3391–3395 (1982).
63. A. M. Brito-Silva, L. A. Gomez, C. B. de Araújo, and A. Galembeck, “Laser ablated silver nanoparticles with nearly the same size in different carrier media,” J. Nanomater. **2010**, 1–7 (2010).
64. M. Sheik-Bahae, A. A. Said, T.-H. Wei, D. J. Hagan, and E. W. Van Stryland, “Sensitive measurement of optical nonlinearities using a single beam,” IEEE J. Quantum Electron. **26**, 760–769 (1990).
65. K. Uchida, S. Kaneko, S. Omi, C. Hata, H. Tanji, Y. Asahara, A. J. Ikushima, T. Tokisaki, and A. Nakamura, “Optical nonlinearities of high concentration of small metal particles dispersed in glass: copper and silver particles,” J. Opt. Soc. Am. B **11**, 1236–1243 (1994).
66. R. A. Ganeev, A. I. Ryasnyansky, S. R. Kamalov, M. K. Kodirov, and T. Usmanov, “Nonlinear susceptibilities, absorption coefficients and refractive indices of colloidal metals,” J. Phys. D **34**, 1602–1611 (2001).
67. E. L. Falcão-Filho, C. B. de Araújo, and J. J. Rodrigues, Jr., “High-order nonlinearities of aqueous colloids containing silver nanoparticles,” J. Opt. Soc. Am. B **24**, 2948–2956 (2007).

68. K.-H. Kim, A. Husakou, and J. Herrmann, “Linear and nonlinear optical characteristics of composites containing metal nanoparticles with different sizes and shapes,” Opt. Express **18**, 7488–7496 (2010).
69. Y. Tsutsui, T. Hayakawa, G. Kawamura, and M. Nogami, “Tuned longitudinal surface plasmon resonance and third-order nonlinear optical properties of gold nanorods,” Nanotechnology **22**, 275203 (2011).
70. J. Olesiak-Banska, M. Gordel, R. Kolkowski, K. Matczyszyn, and M. Samoc, “Third-order nonlinear optical properties of colloidal gold nanorods,” J. Phys. Chem. C **116**, 13731–13737 (2012).
71. S. Mohan, J. Lange, H. Graener, and G. Seifert, “Surface plasmon assisted optical nonlinearities of uniformly oriented metal nano-ellipsoids in glass,” Opt. Express **20**, 28655–28663 (2012).
72. J. Jayabalan, A. Singh, S. Khan, and R. Chari, “Third-order nonlinearity of metal nanoparticles: isolation of instantaneous and delayed contributions,” J. Appl. Phys. **112**, 103524 (2012).
73. S. Mohapatra, Y. K. Mishra, A. M. Warrier, R. Philip, S. Sahoo, A. K. Arora, and D. K. Avasthi, “Plasmonic, low-frequency Raman, and nonlinear optical-limiting studies in copper-silica nanocomposites,” Plasmonics **7**, 25–31 (2012).
74. R. A. Ganeev, *Nonlinear Optical Properties of Materials* (Springer, 2013).
75. R. Kuladeep, K. S. Alee, L. Jyothi, and D. N. Rao, “Synthesis, characterization and nonlinear optical properties of laser-induced Au coloidal nanoparticles,” Adv. Mater. Lett. **4**, 482–487 (2013).
76. L.-D. Wang, T. Zhang, X.-Y. Zhang, Y.-J. Song, R.-Z. Li, and S.-Q. Zhu, “Optical properties of Ag nanoparticle-polymer composite film based on two-dimensional Au nanoparticle array film,” Nano. Res. Lett. **9**, 155–167 (2014).
77. B. Can-Uc, R. Rangel-Rojo, A. Peña-Ramírez, C. B. de Araújo, H. T. M. C. M. Baltar, A. Crespo-Sosa, M. L. Garcia-Betancourt, and A. Oliver, “Nonlinear optical response of platinum nanoparticles and platinum ions embedded in sapphire,” Opt. Express **24**, 9955–9965 (2016).
78. C. B. de Araújo, L. R. P. Kassab, C. T. Dominguez, S. J. L. Ribeiro, A. S. L. Gomes, and A. S. Reyna, “Photoluminescence and nonlinear optical phenomena in plasmonic random media: a review of recent works,” J. Lumin. **169**, 492–496 (2016).
79. C. B. de Araújo, A. S. L. Gomes, and G. Boudebs, “Techniques for nonlinear optical characterization of materials: a review,” Rep. Prog. Phys. **79**, 036401 (2016).
80. E. L. Falcão-Filho, R. Barbosa-Silva, R. G. Sobral-Filho, A. M. Brito-Silva, A. Galembeck, and C. B. de Araújo, “High-order nonlinearity of silica-gold nanoshells in chloroform at 1560 nm,” Opt. Express **18**, 21636–21644 (2010).
81. J. Jayabalan, “Origin and time dependence of higher-order nonlinearities in metal nanocomposites,” J. Opt. Soc. Am. B **28**, 2448–2455 (2011).
82. J. P. Huang and K. W. Yu, “Enhanced nonlinear optical responses of materials: composite effects,” Phys. Rep. **431**, 87–172 (2006).
83. M. A. Vincent and D. de Ceglia, “Effective medium theories,” in *Fundamentals and Applications of Nanophotonics*, J. W. Haus, ed. (Elsevier, 2016), pp. 211.
84. T. C. Choy, *Effective Medium Theory: Principles and Applications in Fundamentals and Applications of Nanophotonics* (Oxford University, 2016).
85. V. A. Markel, “Introduction to the Maxwell-Garnett approximation: tutorial,” J. Opt. Soc. Am. A **33**, 1244–1256 (2016).
86. V. A. Markel, “Maxwell-Garnet approximation (advanced topics): tutorial,” J. Opt. Soc. Am. A **33**, 2237–2255 (2016).

87. D. A. G. Bruggeman, “Berechnung verschiedener physikalischer Konstanten von heterogenen Substanzen. I. Dielektrizitätskonstanten und Leitfähigkeiten der Mischkörper aus isotropen Substanzen,” Annalen der Physik **416**, 636–664 (1935).
88. R. J. Gehr and R. W. Boyd, “Optical properties of nanostructured optical materials,” Chem. Mater. **8**, 1807–1819 (1996).
89. O. Levy and D. Stroud, “Maxwell Garnett theory for mixtures of anisotropic inclusions: application to conducting polymers,” Phys. Rev. B **56**, 8035–8046 (1997).
90. B. N. J. Persson and A. Liebsch, “Optical properties of inhomogeneous media,” Solid State Commun. **44**, 1637–1640 (1982).
91. R. J. Elliott, J. A. Krumhansl, and P. L. Leath, “The theory and properties of randomly disordered crystals and related physical systems,” Rev. Mod. Phys. **46**, 465–543 (1974).
92. J. R. Birchak, L. G. Gardner, J. W. Hipp, and J. M. Victor, “High dielectric constant microwave probes for sensing soil moisture,” Proc. IEEE **62**, 93–98 (1974).
93. H. Looyenga, “Dielectric constants of mixtures,” Physica **31**, 401–406 (1965).
94. J. E. Sipe and R. W. Boyd, “Nonlinear susceptibility of composite optical materials in the Maxwell-Garnet model,” Phys. Rev. A **46**, 1614–1629 (1992).
95. K. Dolgaleva and R. W. Boyd, “Local-field effects in nanostructured photonic materials,” Adv. Opt. Photonics **4**, 1–77 (2012).
96. D. D. Smith, G. Fisher, R. W. Boyd, and D. A. Gregory, “Cancellation of photoinduced absorption in metal nanoparticles composites through a counterintuitive consequence of local field effects,” J. Opt. Soc. Am. B **14**, 1625–1631 (1997).
97. R. J. Gehr, G. L. Fisher, and R. W. Boyd, “Nonlinear-optical response of porous-glass based composite materials,” J. Opt. Soc. Am. B **14**, 2310–2314 (1997).
98. A. S. Reyna and C. B. de Araújo, “Spatial phase modulation due to quintic and septic nonlinearities in metal colloids,” Opt. Express **22**, 22456–22469 (2014).
99. N. C. Kothari, “Effective-medium theory of a nonlinear composite medium using the T-matrix approach: exact results for spherical grains,” Phys. Rev. A **41**, 4486–4492 (1990).
100. P. N. Butcher and D. Cotter, *The Elements of Nonlinear Optics* (Cambridge University, 1990).
101. E. L. Falcão-Filho, C. B. de Araújo, A. Galembeck, M. M. Oliveira, and A. J. G. Zarbin, “Nonlinear susceptibility of colloids consisting of silver nanoparticles in carbon disulfide,” J. Opt. Soc. Am. B **22**, 2444–2449 (2005).
102. M. Centurion, M. A. Porter, P. G. Kevrekidis, and D. Psaltis, “Nonlinearity management in optics: experiment, theory, and simulation,” Phys. Rev. Lett. **97**, 033903 (2006).
103. I. Towers and B. A. Malomed, “Stable (2 + 1)-dimensional solitons in a layered medium with sign-alternating Kerr nonlinearity,” J. Opt. Soc. Am. B **19**, 537–543 (2002).
104. H. Saito and M. Ueda, “Dynamically stabilized bright solitons in a two-dimensional Bose-Einstein condensate,” Phys. Rev. Lett. **90**, 040403 (2003).
105. A. S. Reyna and C. B. de Araújo, “Nonlinearity management of photonic composites and observation of spatial-modulation instability due to quintic nonlinearity,” Phys. Rev. A **89**, 063803 (2014).
106. H. P. S. Castro, H. Wender, M. A. R. C. Alencar, S. R. Teixeira, J. Dupont, and J. M. Hickmann, “Third-order nonlinear optical response of colloidal gold nanoparticles prepared by sputtering deposition,” J. Appl. Phys. **114**, 183104 (2013).
107. R. del Coso, J. Requejo-Isidro, J. Solis, J. Gonzalo, and C. N. Afonso, “Third order nonlinear optical susceptibility of Cu:$Al_2O_3$ nanocomposites: from

spherical nanoparticles to the percolation threshold," J. Appl. Phys. **95**, 2755–2762 (2004).
108. M. Reichert, H. Hu, M. R. Ferdinandus, M. Seidel, P. Zhao, T. R. Ensley, D. Peceli, J. M. Reed, D. A. Fishman, S. Webster, D. J. Hagan, and E. W. V. Stryland, "Temporal, spectral, and polarization dependence of the nonlinear optical response of carbon disulfide," Optica **1**, 436–445 (2014).
109. R. Sato, M. Ohnuma, K. Oyoshi, and Y. Takeda, "Experimental investigation of nonlinear optical properties of Ag nanoparticles: effects of size quantization," Phys. Rev. B **90**, 125417 (2014).
110. M. Segev, Y. Silberberg, and D. N. Christodoulides, "Anderson localization of light," Nat. Photonics **7**, 197–204 (2013).
111. S. Toroghi and P. G. Kik, "Cascaded plasmonic metamaterials for phase-controlled enhancement of nonlinear absorption and refraction," Phys. Rev. B **85**, 045432 (2012).
112. H. A. Atwater and A. Polman, "Plasmonics for improved photovoltaic devices," Nat. Mater. **9**, 205–213 (2010).
113. C. F. Guo, T. Sun, F. Cao, Q. Liu, and Z. Ren, "Metallic nanostructure for light trapping in energy-harvesting devices," Light Sci. Appl. **3**, e161 (2014).
114. Y. R. Shen, *The Principles of Nonlinear Optics* (Wiley, 1984).
115. W. R. Callen, B. G. Huth, and R. H. Pantell, "Optical patterns of thermally self-defocused light," Appl. Phys. Lett. **11**, 103–105 (1967).
116. F. W. Dabby, T. K. Gustafson, J. R. Whinnery, Y. Kohanzadeh, and P. L. Kelley, "Thermally self-induced phase modulation of laser beams," Appl. Phys. Lett. **16**, 362–365 (1970).
117. K. Ogusu, Y. Kohtani, and H. Shao, "Laser-induced diffraction rings from an absorbing solution," Opt. Rev. **3**, 232–234 (1996).
118. R. G. Harrison, L. Dambly, D. Yu, and W. Lu, "A new self-diffraction pattern formation in defocusing liquid media," Opt. Commun. **139**, 69–72 (1997).
119. V. Pilla, E. Munin, and M. R. R. Gesualdi, "Measurement of the thermo-optic coefficient in liquids by laser-induced conical diffraction and thermal lens techniques," J. Opt. A **11**, 105201 (2009).
120. R. Karimzadeh, H. Aleali, and N. Mansour, "Thermal nonlinear refraction properties of $Ag_2S$ semiconductor nanocrystals with its application as a low power optical limiter," Opt. Commun. **284**, 2370–2375 (2011).
121. J. Z. Anvari, R. Karimzadeh, and N. Mansour, "Thermo-optic properties and nonlinear responses of copper nanoparticles in polysiloxane oil," J. Opt. **12**, 035212 (2010).
122. Y. E. Geints, N. S. Panamarev, and A. A. Zemlyanov, "Transient behavior of far-field diffraction patterns of a Gaussian laser beam due to the thermo-optical effect in metal nanocolloids," J. Opt. **13**, 055707 (2011).
123. Z. Mao, L. Qiao, F. He, Y. Liao, C. Wang, and Y. Cheng, "Thermal-induced nonlinear optical characteristics of ethanol solution doped with silver nanoparticles," Chin. Opt. Lett. **7**, 949–952 (2009).
124. C. M. Nascimento, M. A. R. C. Alencar, S. Chávez-Cerda, M. G. A. da Silva, M. R. Meneghetti, and J. M. Hickmann, "Experimental demonstration of novel effects on the far-field diffraction patterns of a Gaussian beam in a Kerr medium," J. Opt. A **8**, 947–951 (2006).
125. M. H. M. Ara, Z. Dehghani, R. Sahraei, A. Daneshfar, Z. Javadi, and F. Divsar, "Diffraction patterns and nonlinear optical properties of gold nanoparticles," J. Quant. Spectrosc. Radiat. Transfer **113**, 366–372 (2012).
126. R. Zamiri, A. Zakaria, M. B. Ahmad, A. R. Sadrolhosseini, K. Shameli, M. Darroudi, and M. A. Mahdi, "Investigation of spatial self-phase modulation

of silver nanoparticles in clay suspension," Optik (Stuttgart) **122**, 836–838 (2011).

127. H.-J. Zhang, J.-H. Dai, P.-Y. Wang, and L.-A. Wu, "Self-focusing and self-trapping in new types of Kerr media with large nonlinearities," Opt. Lett. **14**, 695–696 (1989).
128. W. Wan, S. Jia, and J. W. Fleischer, "Dispersive superfluid-like shock waves in nonlinear optics," Nat. Phys. **3**, 46–51 (2007).
129. S. D. Durbin, S. M. Arakelian, and Y. R. Shen, "Laser-induced diffraction rings from a nematic-liquid-crystal film," Opt. Lett. **6**, 411–413 (1981).
130. N. F. Pilipetski, A. V. Sukhov, N. V. Tabiryan, and B. Y. Zel'dovich, "The orientational mechanism of nonlinearity and the self-focusing of He-Ne laser radiation in nematic liquid crystal mesophase (theory and experiment)," Opt. Commun. **37**, 280–284 (1981).
131. E. Santamato and Y. R. Shen, "Field-curvature effect on the diffraction ring pattern of a laser beam dressed by spatial self-phase modulation in a nematic film," Opt. Lett. **9**, 564–566 (1984).
132. G. Wang, S. Zhang, F. A. Umran, X. Cheng, N. Dong, D. Coghlan, Y. Cheng, L. Zhang, W. J. Blau, and J. Wang, "Tunable effective nonlinear refractive index of graphene dispersions during the distortion of spatial self-phase modulation," Appl. Phys. Lett. **104**, 141909 (2014).
133. T. Myint and R. R. Alfano, "Spatial phase modulation from permanent memory in doped glass," Opt. Lett. **35**, 1275–1277 (2010).
134. D. Grischkowsk, "Self-focusing of light by potassium vapor," Phys. Rev. Lett. **24**, 866–869 (1970).
135. M. Trejo-Durán, J. A. Andrade-Lucio, A. Martínez-Richa, R. Vera-Graziano, and V. M. Castaño, "Self-diffracting effects in hybrid materials," Appl. Phys. Lett. **90**, 091112 (2007).
136. S. Prusty, H. S. Mavi, and A. K. Shukla, "Optical nonlinearity in silicon nanoparticles: effect of size and probing intensity," Phys. Rev. B **71**, 113313 (2005).
137. L. Deng, K. He, T. Zhou, and C. Li, "Formation and evolution of far-field diffraction patterns of divergent and convergent Gaussian beams passing through self-focusing and self-defocusing media," J. Opt. A **7**, 409–415 (2005).
138. S. Wen and D. Fan, "Spatiotemporal instabilities in nonlinear Kerr media in the presence of arbitrary higher-order dispersions," J. Opt. Soc. Am. B **19**, 1653–1659 (2002).
139. V. K. Sharma, A. Goyal, T. S. Raju, C. N. Kumar, and P. K. Panigrahi, "Spatial, temporal, and spatio-temporal modulational instabilities in a planar dual-core waveguide," Opt. Fiber Technol. **24**, 119–126 (2015).
140. Y. S. Kivshar, D. Anderson, and M. Lisak, "Modulation instabilities and dark solitons in a generalized nonlinear Schrödinger equation," Phys. Scripta **47**, 679–681 (1993).
141. N. N. Rozanov, "Modulation instability in a medium with a nonlocal nonlinearity," Opt. Spectrosc. **100**, 609–612 (2006).
142. B. K. Esbensen, A. Wlotzka, M. Bache, O. Bang, and W. Krolikowski, "Modulational instability and solitons in nonlocal media with competing nonlinearities," Phys. Rev. A **84**, 053854 (2011).
143. D. Kip, M. Soljačić, M. Segev, S. M. Sears, and D. N. Christodoulides, "(1 + 1)-Dimensional modulation instability of spatially incoherent light," J. Opt. Soc. Am. B **19**, 502–512 (2002).
144. Z. Liu, S. Liu, R. Guo, Y. Gao, X. Qi, L. Zhou, and Y. Li, "Modulation instability with incoherent white light in self-defocusing photorefractive crystal," Opt. Commun. **281**, 3171–3176 (2008).

145. V. I. Bespalov and V. I. Talanov, “Filamentary structure of light beams in nonlinear liquids,” J. Exp. Theor. Phys. Lett. **3**, 307–310 (1966).
146. W.-P. Hong, “Modulational instability of optical waves in the high dispersive cubic-quintic nonlinear Schrödinger equation,” Opt. Commun. **213**, 173–182 (2002).
147. R. Gupta, T. S. Raju, C. N. Kumar, and P. K. Panigrahi, “Modulational instability of copropagating light beams induced by cubic-quintic nonlinearity in nonlinear negative-index material,” J. Opt. Soc. Am. B **29**, 3360–3366 (2012).
148. M. Saha and A. K. Sarma, “Modulation instability in nonlinear metamaterials induced by cubic-quintic nonlinearities and higher order dispersive effects,” Opt. Commun. **291**, 321–325 (2013).
149. H. Tagwo, C. G. L. Tiofack, O. Dafounansou, A. Mohamadou, and T. C. Kofane, “Effect of competing cubic-quintic nonlinearities on the modulational instability in nonlocal Kerr-type media,” J. Mod. Opt. **63**, 558–565 (2016).
150. G. P. Agrawal, “Induced focusing of optical beams in self-defocusing media,” Phys. Rev. Lett. **64**, 2487–2490 (1990).
151. J. M. Hickmann, A. S. L. Gomes, and C. B. de Araújo, “Observation of spatial cross-phase modulation effects in a self-defocusing nonlinear medium,” Phys. Rev. Lett. **68**, 3547–3550 (1992).
152. K. V. Peddanarappagari and M. Brandt-Pearce, “Volterra series transfer function of single-mode fibers,” J. Lightwave Technol. **15**, 2232–2241 (1997).
153. R. Y. Chiao, E. Garmire, and C. H. Townes, “Self-trapping of optical beams,” Phys. Rev. Lett. **13**, 479–482 (1964).
154. G. I. Stegeman and M. Segev, “Optical spatial solitons and their interactions: universality and diversity,” Science **286**, 1518–1523 (1999).
155. Y. Kivshar, “Spatial solitons: bending light at will,” Nat. Phys. **2**, 729–730 (2006).
156. Z. Chen, M. Segev, and D. N. Christodoulides, “Optical spatial solitons: historical overview and recent advances,” Rep. Prog. Phys. **75**, 086401 (2012).
157. A. Barthelemy, S. Maneuf, and C. Froehly, “Propagation soliton et auto-confinement de faisceaux laser par non linearité optique de kerr,” Opt. Commun. **55**, 201–206 (1985).
158. J. S. Aitchison, A. M. Weiner, Y. Silberberg, M. K. Oliver, J. L. Jackel, D. E. Leaird, E. M. Vogel, and P. W. E. Smith, “Observation of spatial optical solitons in a nonlinear glass waveguide,” Opt. Lett. **15**, 471–473 (1990).
159. P. L. Kelley, “Self-focusing of optical beams,” Phys. Rev. Lett. **15**, 1005–1008 (1965).
160. E. L. Dawes and J. H. Marburger, “Computer studies in self-focusing,” Phys. Rev. **179**, 862–868 (1969).
161. J. H. Marburger, “Self-focusing: theory,” Prog. Quantum Electron. **4**, 35–110 (1975).
162. N. Akhmediev and J. M. Soto-Crespo, “Generation of a train of three-dimensional optical solitons in a self-focusing medium,” Phys. Rev. A **47**, 1358–1364 (1993).
163. R. Carretero-Gonzáles, J. D. Talley, C. Chong, and B. A. Malomed, “Multistable solitons in the cubic-quintic discrete nonlinear Schrödinger equation,” Phys. D **216**, 77–89 (2006).
164. D. Mihalache, D. Mazilu, F. Lederer, H. Leblond, and B. A. Malomed, “Stability of dissipative optical solitons in the three-dimensional cubic-quintic Ginzburg-Landau equation,” Phys. Rev. A **75**, 033811 (2007).
165. D. Mihalache, D. Mazilu, F. Lederer, B. Malomed, Y. Kartashov, L.-C. Crasovan, and L. Torner, “Three-dimensional spatiotemporal optical solitons in nonlocal nonlinear media,” Phys. Rev. E **73**, 025601(R) (2006).

166. G. Fibich, “Self-focusing in the damped nonlinear Schrödinger equation,” SIAM J. Appl. Math. **61**, 1680–1705 (2001).
167. T. Passota, C. Sulem, and P. L. Sulem, “Linear versus nonlinear dissipation for critical NLS equation,” Phys. D **203**, 167–184 (2005).
168. E. L. Falcão-Filho, C. B. de Araújo, G. Boudebs, H. Leblond, and V. Skarka, “Robust two-dimensional spatial solitons in liquid carbon disulfide,” Phys. Rev. Lett. **110**, 013901 (2013).
169. Z. Wu, Y. Zhang, C. Yuan, F. Wen, H. Zheng, and Y. Zhang, “Cubic-quintic condensate solitons in four-wave mixing,” Phys. Rev. A **88**, 063828 (2013).
170. A. Pasquazi, M. Peccianti, M. Clerici, C. Conti, and R. Morandotti, “Collapse arrest in instantaneous Kerr media via parametric interactions,” Phys. Rev. Lett. **113**, 133901 (2014).
171. A. S. Reyna, K. C. Jorge, and C. B. de Araújo, “Two-dimensional solitons in a quintic-septimal medium,” Phys. Rev. A **90**, 063835 (2014).
172. K. C. Jorge, R. Riva, N. A. S. Rodrigues, J. M. S. Sakamoto, and M. G. Destro, “Scattered light imaging method (SLIM) for characterization of arbitrary laser beam intensity profiles,” Appl. Opt. **53**, 4555–4564 (2014).
173. K. C. Jorge, H. A. García, A. M. Amaral, A. S. Reyna, L. S. Menezes, and C. B. de Araújo, “Measurements of the nonlinear refractive index in scattering media using the scattered light imaging method—SLIM,” Opt. Express **23**, 19512–19521 (2015).
174. Y. Chung and P. M. Lushnikov, “Strong collapse turbulence in a quintic nonlinear Schrödinger equation,” Phys. Rev. E **84**, 036602 (2011).
175. A. S. Reyna, B. A. Malomed, and C. B. de Araújo, “Stability conditions for one-dimensional optical solitons in cubic-quintic-septimal media,” Phys. Rev. A **92**, 033810 (2015).
176. Y. S. Kivshar and B. Luther-Davies, “Dark optical solitons: physics and applications,” Phys. Rep. **298**, 81–197 (1998).
177. A. S. Desyatnikov, Y. S. Kivshar, and L. Torner, “Optical vortices and vortex solitons,” Prog. Opt. **47**, 291–391 (2005).
178. Y. S. Kivshar, “Dark solitons in nonlinear optics,” IEEE J. Quantum Electron. **29**, 250–264 (1993).
179. G. A. Swartzlander, Jr., D. R. Andersen, J. J. Regan, H. Yin, and A. E. Kaplan, “Spatial dark-soliton stripes and grids in self-defocusing materials,” Phys. Rev. Lett. **66**, 1583–1586 (1991).
180. E. A. Kuznetsov and S. K. Turitsyn, “Instability and collapse of solitons in media with a defocusing nonlinearity,” J. Exp. Theor. Phys. **67**, 1583–1588 (1988).
181. V. Tikhonenko, J. Christou, B. Luther-Davies, and Y. S. Kivshar, “Observation of vortex solitons created by the instability of dark soliton stripes,” Opt. Lett. **21**, 1129–1131 (1996).
182. A. M. Yao and M. J. Padgett, “Orbital angular momentum: origins, behavior and applications,” Adv. Opt. Photon. **3**, 161–204 (2011).
183. A. M. Amaral, E. L. Falcão-Filho, and C. B. de Araújo, “Characterization of topological charge and orbital angular momentum of shaped optical vórtices,” Opt. Express **22**, 30315–30324 (2014).
184. G. A. Swartzlander, Jr. and C. T. Law, “Optical vortex solitons observed in Kerr nonlinear media,” Phys. Rev. Lett. **69**, 2503–2506 (1992).
185. Y. S. Kivshar and G. P. Agrawal, *Optical Solitons: From Fibers to Photonic Crystals* (Academic, 2003).
186. R. Passier, M. Chauvet, B. Wacogne, and F. Devaux, “Light-induced waveguide by a finite self-trapped vortex beam in a photorefractive medium,” J. Opt. **13**, 085502 (2011).

187. C. T. Law, X. Zhang, and G. A. Swartzlander, “Waveguiding properties of optical vortex solitons,” Opt. Lett. **25**, 55–57 (2000).
188. A. S. Reyna and C. B. de Araújo, “Guiding and confinement of light induced by optical vortex solitons in a cubic-quintic medium,” Opt. Lett. **41**, 191–194 (2016).
189. G. P. Agrawal, “Nonlinear fiber optics: its history and recent progress,” J. Opt. Soc. Am. B **28**, A1–A10 (2011).
190. A. Lin, X. Liu, P. R. Watekar, W. Zhao, B. Peng, C. Sun, Y. Wang, and W.-T. Han, “All-optical switching application of germane-silicate optical fiber incorporated with Ag nanocrystals,” Opt. Lett. **34**, 791–793 (2009).
191. R. Chattopadhyay and S. K. Bhadra, “Dispersion tailoring in single mode optical fiber by doping silver nanoparticles,” Appl. Phys. B **111**, 399–406 (2013).
192. R. E. P. de Oliveira, N. Sjödin, M. Fokine, W. Margulis, C. J. S. de Matos, and L. Norin, “Fabrication and optical characterization of silica optical fibers containing gold nanoparticles,” ACS Appl. Mater. Interface **7**, 370–375 (2015).
193. J. F. Algorri, D. Poudereux, B. García-Cámara, V. Urruchi, J. M. Sánchez-Pena, R. Vergaz, M. Caño-García, X. Quintana, M. A. Geday, and J. M. Otón, “Metal nanoparticles–PDMS nanocomposites for tunable optical filters and sensors,” Opt. Data Process. Storage **2**, 1–6 (2016).
194. G. P. Agrawal, *Nonlinear Fiber Optics* (Academic, 2013).
195. P. D. Maker, R. W. Terhune, and C. M. Savage, “Intensity-dependent changes in the refractive index of liquids,” Phys. Rev. Lett. **12**, 507–509 (1964).
196. A. M. Kokhkharov, S. A. Bakhramov, U. K. Makhmanov, R. A. Kokhkharov, and E. A. Zakhidov, “Self-induced polarization rotation of laser beam in fullerene ($C_{70}$) solutions,” Opt. Commun. **285**, 2947–2951 (2012).
197. J. Borhanian, “Nonlinear birefringence in plasmas: polarization dynamics, vector modulational instability, and vector solitons,” Phys. Plasmas **21**, 062312 (2014).
198. P. S. Eldridge, P. G. Lagoudakis, M. Henini, and R. T. Harley, “Nonlinear birefringence and time-resolved Kerr measurement of spin lifetimes in (110) $GaAs/Al_yGa_{1-y}As$ quantum wells,” Phys. Rev. B **81**, 033302 (2010).
199. A. N. Korolevich and M. Belsley, “Simultaneous measurements of thermally induced birefringence and thermal refraction in absorptive glass filters,” J. Opt. B **3**, S173–S179 (2001).
200. R. Kashiap and N. Finlayson, “Nonlinear polarization coupling and instabilities in single-mode liquid-cored optical fibers,” Opt. Lett. **17**, 405–407 (1992).
201. V. Loriot, E. Hertz, O. Faucher, and B. Lavorel, “Measurement of high order Kerr refractive index of major air components,” Opt. Express **17**, 13429–13434 (2009).
202. G. Stegeman, D. G. Papazoglou, R. Boyd, and S. Tzortzakis, “Nonlinear birefringence due to non-resonant, higher-order Kerr effect in isotropic media,” Opt. Express **19**, 6387–6399 (2011).
203. H. G. Winful, “Polarization instabilities in birefringent nonlinear media: application to fiber-optic devices,” Opt. Lett. **11**, 33–35 (1986).
204. S. Trillo, S. Wabnitz, R. H. Stolen, G. Assanto, C. T. Seaton, and G. I. Stegeman, “Experimental observation of polarization instability in a birefringent optical fiber,” Appl. Phys. Lett. **49**, 1224–1226 (1986).
205. A. S. Reyna, E. Bergmann, P.-F. Brevet, and C. B. de Araújo, “Nonlinear polarization instability in cubic-quintic photonic nanocomposites,” Opt. Express **25**, 21049–21067 (2017).
206. O. Wada, “Femtosecond all-optical devices for ultrafast communication and signal processing,” New J. Phys. **6**, 183 (2004).
207. V. Mizrahi, K. W. Delong, G. I. Stegeman, M. A. Saifi, and M. J. Andrejco, “Two-photon absorption as a limitation to all-optical switching,” Opt. Lett. **14**, 1140–1142 (1989).

208. S. R. Friberg and P. W. Smith, “Nonlinear optical glasses for ultrafast optical switches,” IEEE J. Quantum Electron. **23**, 2089–2094 (1987).
209. G. I. Stegeman, E. M. Wright, N. Finlayson, and R. Zanoni, “Third order nonlinear integrated optics,” J. Mater. Sci. **33**, 2235–2249 (1998).
210. A. S. Reyna and C. B. de Araújo, “An optimization procedure for the design of all-optical switches based on metal-dielectric nanocomposites,” Opt. Express **23**, 7659–7666 (2015).
211. M. A. Duguay and J. W. Hansen, “An ultrafast light gate,” Appl. Phys. Lett. **15**, 192–194 (1969).
212. M. H. G. Miranda, E. L. Falcão-Filho, J. J. Rodrigues, Jr., C. B. de Araújo, and L. H. Acioli, “Ultrafast light-induced dichroism in silver nanoparticles,” Phys. Rev. B **70**, 161401(R) (2004).
213. J. Zeng and B. A. Malomed, “Stabilization of one-dimensional solitons against the critical collapse by quintic nonlinear lattices,” Phys. Rev. A **85**, 023824 (2012).
214. B. B. Baizakov, B. A. Malomed, and M. Salerno, “Multidimensional solitons in periodic potentials,” Europhys. Lett. **63**, 642–648 (2003).
215. D. E. Pelinovsky, Y. S. Kivshar, and V. V. Afanasjev, “Internal modes of envelope solitons,” Phys. D **116**, 121–142 (1998).
216. J. Zeng and B. A. Malomed, “Bright solitons in defocusing media with spatial modulation of the quintic nonlinearity,” Phys. Rev. E **86**, 036607 (2012).
217. N. G. Vakhitov and A. A. Kolokolov, “Stationary solutions of the wave equation in a medium with nonlinearity saturation,” Radiophys. Quantum Electron. **16**, 783–789 (1973).
218. S. Wang and L. Zhang, “An efficient split-step compact finite difference method for cubic-quintic complex Ginzburg-Landau equations,” Comp. Phys. Commun. **184**, 1511–1521 (2013).
219. R. El-Ganainy, D. N. Christodoulides, C. Rotschild, and M. Segev, “Soliton dynamics and self-induced transparency in nonlinear nanosuspensions,” Opt. Express **15**, 10207–10218 (2007).
220. J. D. Jackson, *Classical Electrodynamics* (Wiley, 1998).
221. T. S. Kelly, Y.-X. Ren, A. Samadi, A. Bezryadina, D. Christodoulides, and Z. Chen, “Guiding and nonlinear coupling of light in plasmonic nanosuspensions,” Opt. Lett. **41**, 3817–3820 (2016).
222. V. Skarka, N. B. Aleksić, W. Krolikowski, D. N. Christodoulides, S. Rakotoarimalala, B. N. Aleksić, and M. Belić, “Self-structuring of stable dissipative breathing vortex solitons in a colloidal nanosuspension,” Opt. Express **25**, 10090–10102 (2017).
223. D. R. Smith, J. B. Pendry, and M. C. K. Wiltshire, “Metamaterials and negative refractive index,” Science **305**, 788–792 (2004).
224. R. A. Shelby, D. R. Smith, and S. Schultz, “Experimental verification of a negative index of refraction,” Science **292**, 77–79 (2001).
225. J. Chen, Y. Wang, B. Jia, T. Geng, X. Li, L. Feng, W. Qian, B. Liang, X. Zhang, M. Gu, and S. Zhuang, “Observation of the inverse Doppler effect in negative-index materials at optical frequencies,” Nat. Photonics **5**, 239–245 (2011).
226. M. Lapine, I. V. Shadrivov, and Y. S. Kivshar, “Colloquium: nonlinear metamaterials,” Rev. Mod. Phys. **86**, 1093–1123 (2014).
227. K. Yao and Y. Liu, “Plasmonic metamaterials,” Nanotechnol. Rev. **3**, 177–192 (2014).
228. H. Husu, R. Siikanen, J. Mäkitalo, J. Lehtolahti, J. Laukkanen, M. Kuittinen, and M. Kauranen, “Metamaterials with tailored nonlinear optical response,” Nano Lett. **12**, 673–677 (2012).

229. M. Gentile, M. Hentschel, R. Taubert, H. Guo, H. Giessen, and M. Fiebig, "Investigation of the nonlinear optical properties of metamaterials by second harmonic generation," Appl. Phys. B **105**, 149–162 (2011).
230. J. B. Khurgin and G. Sun, "Third-order nonlinear plasmonic materials: enhancement and limitations," Phys. Rev. A **88**, 053838 (2013).
231. Y. Liu, Y. L. Xue, and C. Yu, "Modulation instability induced by cross-phase modulation in negative index materials with higher-order nonlinearity," Opt. Commun. **339**, 66–73 (2015).
232. Q. Zhou, L. Liu, Y. Liu, H. Yu, P. Yao, C. Wei, and H. Zhang, "Exact optical solitons in metamaterials with cubic-quintic nonlinearity and third-order dispersion," Nonlinear Dyn. **80**, 1365–1371 (2015).
233. Q. Zhou, Q. Zhu, Y. Liu, H. Yu, Z. Wu, J. Lu, C. Wei, and A. Biswas, "Analytical study of combo-solitons in optical metamaterials with cubic-quintic nonlinearity," J. Comput. Theor. Nanosci. **12**, 5278–5282 (2015).
234. B. G. O. Essama, J. Atangana, B. M. Frederick, B. Mokhtari, N. C. Eddeqaqi, and T. C. Kofane, "Rogue wave train generation in a metamaterial induced by cubic-quintic nonlinearities and second-order dispersion," Phys. Rev. E **90**, 032911 (2014).
235. J. Zhang, Y. Li, Y. Xiang, D. Lei, and L. Zhang, "Collapse of optical wave by cross-phase modulation in nonlinear metamaterials," J. Mod. Opt. **63**, 605–612 (2016).
236. M. Scalora, M. S. Syrchin, N. Akozbek, E. Y. Poliakov, G. D'Aguanno, N. Mattiucci, M. J. Bloemer, and A. M. Zheltikov, "Generalized nonlinear Schrödinger equation for dispersive susceptibility and permeability: application to negative index materials," Phys. Rev. Lett. **95**, 013902 (2005).
237. R. Yang and Y. Zhang, "Exact combined solitary wave solutions in nonlinear metamaterials," J. Opt. Soc. Am. B **28**, 123–127 (2011).
238. A. D. Boardman, R. C. Mitchell-Thomas, N. J. King, and Y. G. Rapoport, "Bright spatial solitons in controlled negative phase metamaterials," Opt. Commun. **283**, 1585–1597 (2010).

**Albert S. Reyna** received a first-class bachelor's degree in physics from the Universidad Nacional del Callao, Peru and a Master of Science degree in Physics from Universidade Federal de Pernambuco, Brazil. He has recently received the Doctor of Science degree from the Universidade Federal de Pernambuco, working under the supervision of Prof. Cid B. de Araújo on various projects related to high-order nonlinearities in photonic materials, their characterizations, theoretical fundamentals, numerical simulations, and applications. Currently, he is developing a postdoctoral project with focus on the manipulation of light-by-light using intense short light pulses in highly nonlinear materials.

**Cid B. de Araújo** is Emeritus Professor at the Universidade Federal de Pernambuco (UFPE) at Recife (Brazil). He received a B.Sc. degree in electrical engineering from the UFPE and Master of Science and Doctor of Science degrees in physics from the Pontifical Catholic University of Rio de Janeiro (Brazil). He was a research associate at Harvard University (Massachusetts), visiting scientist at the IBM Thomas J. Watson Research Center (New York), visiting researcher at the École Polytechnique

(Palaiseau, France), the Université Paris-Nord (France), and visiting researcher and invited professor at the Université d' Angers (France) on various occasions. At the beginning of his carrier he worked with microwave spectroscopy and optical properties of magnetic materials. His research over the last 40 years has been concentrated in laser spectroscopy of materials, nonlinear optics, and photonics. He guided 77 graduate students and post-doctors. He has authored or co-authored about 300 scientific and technical papers in international journals, 14 book chapters, as well as about 500 contributed and invited conference communications. He was a member of the editorial board of *Applied Physics Letters, Journal of Applied Physics, Optical Materials*, and *Brazilian Journal of Physics*, and he has been a reviewer for various international scientific journals. He is a fellow of The Optical Society (OSA), fellow of The World Academy of Sciences (TWAS), member of the Brazilian Academy of Sciences, member of the Brazilian National Order of Scientific Merit, and member of the Brazilian Physical Society, and he was the recipient of the Galileo Galilei Award 2003 presented by the International Commission for Optics (ICO). He participated in the Membership Advisory Committee for Physics of TWAS, the Commission on Quantum Electronics of the International Union of Pure and Applied Physics (IUPAP), the International Council of the OSA, the Committee for the Galileo Galilei Award of the ICO, several organizing committees of national and international conferences, and various research financial agencies of Brazil, Uruguay, Venezuela, and Chile. Currently he is vice president of the Brazilian Academy of Sciences for the Brazilian Northeast Region.